



1 **PIXAL: A Physics-Informed Explainable Machine Learning Architecture 2 for Greenland Ice Albedo Modeling**

3
4 Raf Antwerpen¹, Marco Tedesco^{1,2}, Pierre Gentine³, Willem Jan van de Berg⁴, and Xavier Fettweis⁵

5
6 ¹ Lamont-Doherty Earth Observatory, Climate School, Columbia University, New York, NY, USA

7 ² NASA Goddard Institute for Space Studies, New York, NY, USA

8 ³ Center for Learning the Earth with Artificial Intelligence and Physics (LEAP), Climate School, Columbia
9 University, New York, NY, USA

10 ⁴ Institute for Marine and Atmospheric Research Utrecht, Utrecht University, Utrecht, the Netherlands

11 ⁵ Department of Geography, University of Liège, Liège, Belgium

12 *Correspondence to:* Raf Antwerpen (ra3063@columbia.edu)

13 **Abstract.** The Greenland ice sheet (GrIS) is a major contributor to global sea level rise. A significant portion of the GrIS' contribution can be attributed to increased ice surface melting, which is strongly controlled by ice albedo, a property that regulates the amount of absorbed solar radiation that leads to surface melting. Yet, we lack a comprehensive understanding of the complex and nonlinear relationships ice albedo has with its environment and is, therefore, often simplified or crudely parameterized in climate models. However, an accurate representation of future ice albedo evolution is essential for reducing uncertainties in sea level rise projections. This study presents PIXAL, a physics-informed explainable machine learning architecture that significantly outperforms the Modèle Atmosphérique Régional (MAR), a state-of-the-art regional climate model, in modeling ice albedo on the southwestern GrIS. PIXAL is based on an Extreme Gradient Boosting (XGBoost) model and is trained on a suite of modeled topographic, atmospheric, radiative, and glaciologic variables from MAR to capture the complex and nonlinear relationships with ice albedo observations obtained from the Moderate Resolution Imaging Spectroradiometer (MODIS). Performance metrics show that PIXAL achieves an R^2 of 0.563, a structural similarity index measure (SSIM) of 0.620, a mean squared error (MSE) of 0.005, and a mean absolute percentage error (MAPE) of 14.699%, compared to MAR's R^2 of 0.062, SSIM of 0.112, MSE of 0.032, and MAPE of 46.202%. Explainable artificial intelligence analysis reveals that topographic features, specifically ice sheet surface height and slope, are the most important drivers of ice albedo variability due to their relationships with ice exposure duration and the effectiveness in accumulating meltwater and light-absorbing constituents (LACs) on flat ice surfaces. Near-surface air temperature and runoff further significantly impact ice albedo variability by affecting the ice metamorphic state and accumulation of meltwater and LACs. These findings highlight that understanding the complex physical processes underlying ice albedo variability is essential for accurate climate modeling and sea level rise predictions. PIXAL represents a crucial advancement in ice albedo modeling and paves the way for improved representation of ice sheets in Earth system models.

33 **1 Introduction**

34 A significant portion of the acceleration of the global mean sea level rise over the last few decades has been attributed to
35 increased surface melting from the Greenland ice sheet (GrIS) (Aschwanden et al., 2019). Climate models project a
36 contribution to global mean sea level rise of 9 to 18 cm from the GrIS by 2100 for the Shared Socioeconomic Pathway SSP5-
37 8.5 (Fox-Kemper et al., 2021; Riahi et al., 2017). The large uncertainty in this projection contributes to the hindrance of



38 accurate and effective mitigation of the implications of sea level change on coastal communities. A large portion of the
39 uncertainty stems from an incomplete understanding of the physical processes that control ice surface melting on the GrIS and
40 their linkages to atmospheric and oceanic processes (van den Broeke et al., 2017). Specifically, we lack an understanding of
41 the spatiotemporal variability of ice albedo, which plays a crucial role in modulating ice surface melt processes (Antwerpen et
42 al., 2022).

43
44 Ice is exposed on the GrIS during the summer melting season (June-August) when increased insolation and increased
45 atmospheric temperature induce melting of the winter snowpack overlying the ice. Snow melt generally occurs in the ablation
46 zone at lower elevations near the ice sheet margin. Here, the surface mass balance is negative, with the ablation of snow and
47 ice (melting, evaporation, and sublimation) being larger than the accumulation (snowfall, rainfall, and refreezing), resulting in
48 a net surface mass loss. Ice melt is strongly controlled by the broadband ice surface albedo, which represents the ratio of
49 reflected (upward) solar radiation flux to incoming (downward) solar radiation flux, weighted by wavelength (visible to near-
50 infrared). For ice, the broadband albedo ranges from ~0.1 to ~0.7 (Klein and Stroeve, 2002; Liang, 2001; Tedstone et al., 2020;
51 Warren and Wiscombe, 1980; Wiscombe and Warren, 1980) while the typical albedo of snow is ~0.7-0.8. The incoming solar
52 radiation that is not reflected by the ice is, instead, absorbed. Because of its lower albedo, a considerably higher amount of
53 incoming solar radiation can be absorbed by ice than by snow. The absorbed radiation heats the surface and shallow subsurface
54 ice and snow layers and induces melting. Meltwater from snow and ice has a low albedo of ~0.1 and when mixed with ice and
55 snow therefore further decreases the albedo, promoting additional melting. This is referred to as the meltwater-albedo feedback
56 (Stroeve, 2001). Under future, warmer atmospheric conditions, snowmelt over the GrIS is expected to increase (Yue et al.,
57 2021). Therefore, the snowline is expected to retreat earlier and further inland, increasing the low-albedo ice areas and
58 accelerating surface melting and sea level rise (Ryan et al., 2019).

59
60 Ice albedo on the GrIS is a highly complex property that is controlled by many factors. The metamorphic state of the surface
61 and shallow subsurface of the ice, determined by ice grain size, density, porosity, specific surface area, and the size and shape
62 of englacial air bubbles, plays a key role in the scattering, absorption, and reflectance of incoming solar radiation (Flanner and
63 Zender, 2006). Moreover, meltwater and rainwater can pond on the ice surface and infiltrate shallow subsurface cavities in the
64 ice, promoting absorption of incoming solar radiation during low cloud-cover days (Tedstone et al., 2020). Solar radiation
65 heats the meltwater and promotes ice melting at the water-ice interface, increasing the presence of meltwater and further
66 darkening the ice sheet. The presence of light-absorbing constituents (LACs), including black carbon, mineral dust, algae, and
67 cryoconite, can significantly lower ice albedo (Goelles and Bøggild, 2017; Hofer et al., 2017; MacGregor et al., 2020;
68 McCutcheon et al., 2021; Williamson et al., 2020). A considerable fraction of LACs that affect GrIS ice albedo are aerosols
69 from distant and local sources (Flanner et al., 2021; Goelles and Bøggild, 2017). Natural sources, including North American,
70 Siberian, and Greenlandic wildfires, emit black carbon particles that have been found on the GrIS (Cali Quaglia et al., 2022;
71 Keegan et al., 2014). Greenlandic wildfires can deposit up to 30% of their emissions onto the ice sheet (Evangelou et al.,
72 2019). Asian and African deserts (Újvári et al., 2022), Icelandic volcanoes (Meinander et al., 2016; Moroni et al., 2018), and
73 Greenlandic ice-free areas (Amino et al., 2021; Nagatsuka et al., 2021) also release dust particles that have been found on the
74 ice sheet. Further, anthropogenic sources, including transportation, industrial, and residential, emit aerosols (Bond et al., 2013),
75 which can be transported across large distances by atmospheric circulations and deposited on the GrIS (Khan et al., 2023;
76 Thomas et al., 2017; Ward et al., 2018). LACs accumulate on the GrIS surface throughout the year and as the snowpack melts
77 during the melting season, LACs can be left behind on the ice and cause darkening while the melted snowpack is flushed out.
78 Additionally, dust accumulated on the GrIS during the last ~15,000 years is melted at the ice surface in the ablation zone,
79 increasing the dust concentration (MacGregor et al., 2020; Wientjes et al., 2012). Moreover, mineral dust provides nutrients
80 for ice algae (McCutcheon et al., 2021). Algal blooms cause a considerable lowering of ice albedo and accelerate surface
81 melting (Cook et al., 2020; Stibal et al., 2017; Wang et al., 2020; Williamson et al., 2020). In areas with heterogeneous ice



82 surfaces, ice roughness and crevasses are also known to significantly influence ice albedo (Cathles et al., 2011). Lastly, a broad
83 swath of environmental and radiative conditions, including temperature, atmospheric composition and circulation, and solar
84 zenith angle, affect the metamorphic state of the ice and the accumulation of LACs and thus play an essential role in controlling
85 ice albedo (Flanner et al., 2021; Hofer et al., 2017; Tedesco et al., 2016).

86
87 The development of a comprehensive and predictive ice albedo model is hindered by a lack of understanding of the drivers of
88 ice albedo, which can lead to underestimates of surface melting and sea level rise (Antwerpen et al., 2022). Typically, Earth
89 system models (ESMs) prescribe constant and uniform values for ice albedo in the visible and near-infrared wavelength regions
90 (van Kampenhout et al., 2020). Recent ice albedo modeling efforts show improved capabilities in representing ice albedo in
91 ESMs and regional climate models (RCMs). For example, through recent improvements, the Snow, Ice, and Aerosol Radiative
92 model (SNICAR), a multi-layer heterogeneous snow albedo radiative transfer model, can now account for the influence of
93 LACs on snow and ice albedo (Flanner et al., 2021; Whicker et al., 2022). SNICAR is currently used in the Energy Exascale
94 Earth System Model (E3SM) and has improved ice albedo and surface melt estimates (Whicker-Clarke et al., 2024). However,
95 due to limitations in quantifying concentrations of individual LACs on the GrIS, the use of SNICAR poses limitations in
96 predicting ice albedo beyond the observational period. The RCM Regional Atmospheric Climate Model (RACMO) approaches
97 this limitation by estimating ice albedo on the GrIS with the 2000-2015 mean broadband ice albedo observations from the
98 Moderate Resolution Imaging Spectroradiometer (MODIS) (van Dalum et al., 2020). While these estimates provide a high ice
99 albedo accuracy during the observation and evaluation period, future changes in environmental and surface conditions on the
100 GrIS may decrease the accuracy of the albedo estimates. Therefore, RACMO may not necessarily employ an accurate
101 representation of ice albedo for end-of-century surface melt projections. The RCM Modèle Atmosphérique Régional (MAR)
102 prescribes ice albedo as a function of accumulated runoff and ice sheet slope, which leads to an overestimation of ice albedo
103 and potential underestimation of meltwater production (Antwerpen et al., 2022). While this model configuration can account
104 for some future changes in environmental and surface conditions, it does not incorporate essential dependencies of ice albedo
105 to environmental variables and, therefore, does not accurately capture the physical processes that underlie ice albedo
106 variability.

107
108 These considerable efforts played important roles in advancing our understanding of ice albedo modeling. Yet, a
109 comprehensive, accurate, and predictive ice albedo model has not yet been developed. Here, we present PIXAL, a Physics-
110 Informed eXplainable machine learning architecture for ice ALbedo modeling. PIXAL is based on an eXtreme Gradient
111 Boosting (XGBoost) model (Chen and Guestrin, 2016) and accurately models and predicts ice albedo on the southwestern
112 GrIS. We extract essential information from the suite of environmental variables modeled by MAR that have previously not
113 been used for ice albedo modeling and train PIXAL to capture the complex and nonlinear relationships between the
114 environment modeled by MAR and the MODIS-derived ice albedo observations. Additionally, we elucidate important
115 environmental drivers of ice albedo by employing SHapley Additive exPlanations (SHAP) (Lundberg and Lee, 2017), an
116 explainable artificial intelligence method. Through this work, we address limitations of ESMs and RCMs in modeling ice
117 albedo on the southwestern GrIS. This includes the dark ice zone, where LACs have a dominant role in controlling ice albedo
118 (Ryan et al., 2018). However, we show that ice albedo modeling improvements can be made even without directly accounting
119 for LACs. Moreover, an improved understanding of the environmental and physical processes underlying ice albedo variability
120 is vital for robust model developments and ice albedo predictions that are stable against uncertain changes in future
121 environmental conditions.



122 **2 Data**

123 **2.1 MAR**

124 We use the Modèle Atmosphérique Régional (MAR) v3.12, an RCM developed to simulate the coupled surface-atmosphere
125 system over polar regions (Fettweis et al., 2017; Gallée, 1997; Lefebvre et al., 2003; Ridder and Schayes, 1997). We run MAR
126 over the GrIS and force the lateral boundaries and ocean surface with 6-h ERA5 reanalysis output (Hersbach et al., 2020),
127 from the European Centre for Medium-Range Weather Forecasts (ECMWF). The atmosphere component of MAR is described
128 by (Gallée and Schayes, 1994) and the surface component is represented by the Soil Ice Snow Vegetation Atmosphere Transfer
129 (SISVAT) scheme (Ridder and Schayes, 1997). The SISVAT scheme includes the Crocus snow model (Brun et al., 1992),
130 which simulates a predefined number of snow, ice, or firn layers with variable thickness and allows energy and mass transport
131 between each layer. Ice albedo (α) is calculated as a function of the model-predicted runoff from melt and rainwater
132 accumulated over the preceding day as:

$$133 \quad \alpha = 0.5 + 0.05 \cdot \frac{1}{e^{\sqrt{\frac{\text{runoff}}{50}}}}, \quad (1)$$

134 In MAR, the ice albedo varies exponentially between a maximum of 0.55 when no surface water is present on the ice surface
135 and a minimum of 0.5 when large amounts of runoff ($> 50 \text{ mmWE}$) are present (Zuo and Oerlemans, 1996). The cumulative
136 runoff is negatively corrected for the ice slope, with steeper ice slopes holding less runoff. MARv3.5.2 is validated over the
137 GrIS (Fettweis et al., 2017) with updates to MARv.311 (Fettweis et al., 2021). Updates to MARv3.12 regarding the base of
138 the snowpack temperature and rainfall to snowfall conversion are provided in (Antwerpen et al., 2022).

139
140 We use MAR to produce daily output of topographic, atmospheric, radiative, and glaciologic variables at its native spatial
141 resolution of 6.5 km: albedo (-), near-surface air temperature ($^{\circ}\text{C}$; average height is 2m), runoff of melt and rain water
142 (mmWE/day), shortwave upward radiation (W/m^2), shortwave downward radiation (W/m^2), longwave upward radiation
143 (W/m^2), longwave downward radiation (W/m^2), sensible heat flux (W/m^2), latent heat flux (W/m^2), cloud cover (down) (-),
144 cloud cover (middle) (-), cloud cover (up) (-), cloud optical depth (-), average ice density of the top 1 m (kg/m^3), zonal wind
145 (m/s), meridional wind (m/s), sublimation (mmWE/day), average liquid water content of the top 1 m (kg/kg), snowfall
146 (mmWE/day), rainfall (mmWE/day), surface height (m), surface slope (degrees), surface aspect (azimuth degrees).

147
148 We select a subset of the MAR output that covers the exposed ice in southwest GrIS during June, July, and August (JJA) in
149 2000-2021. This period encompasses the GrIS melt season when surface albedo has the largest impact on surface melting
150 (Alexander et al., 2014). Following Antwerpen et al. (2022), we distinguish exposed bare ice from snow in MAR as cells
151 where 1) snow is absent and 2) the average ice density of the top 1 m is higher than 907 kg/m^3 . While ice in MAR has a density
152 of 920 kg/m^3 , a thin layer of fresh snowfall with a density of 300 kg/m^3 can lower the average density of the top 1 m to slightly
153 below that of ice without significantly affecting its albedo (Warren et al., 2006). Moreover, using the average ice density
154 ensures ice lenses are not erroneously detected as bare ice. We further constrain ice in MAR to be located below the long-term
155 average equilibrium line altitude (ELA) of 1679 m a.s.l., which represents the 95th percentile value of all sorted elevation
156 values with a negative SMB during JJA of 2000-2021, which denotes the ablation zone.

157 **2.2 MODIS**

158 We collect daily MOD10A1 broadband albedo images (Hall et al., 2016) over the GrIS from the Moderate Resolution Imaging
159 Spectroradiometer (MODIS) for JJA in 2000-2021 at 500 m spatial resolution with Google Earth Engine (Gorelick et al.,
160 2017). We also collect daily MOD09GA v6 band 2 (841-876 nm) surface reflectance images (Vermote and Wolfe, 2015). This



161 product has been corrected for atmospheric conditions, including aerosols, gasses, and Rayleigh scattering. We remove cloud-
162 obstructed pixels using daily MOD10A1 v6 cloud mask images. We average and co-locate the MODIS data to the MAR
163 projection and resolution to allow for a pixel-by-pixel analysis.

164
165 We distinguish exposed bare ice from snow in the MODIS imagery by applying an upper threshold of 0.6 to band 2 of the
166 MOD09GA product (Shimada et al., 2016). We further constrain ice exposure below the long-term average ELA of 1679 m
167 a.s.l. using the static ice mask and digital elevation model (DEM) from the Greenland Ice Mapping Project (GIMP) (Howat et
168 al., 2014). While this may yield a conservative estimate of the ELA during warm high-melt years, we ensure no anomalously
169 high-elevation ablation or cloudy cells erroneously detected as ice are included. The upper threshold of 0.6 may cause some
170 firn to be erroneously detected as ice. Moreover, a thin layer of fresh snowfall over ice may not result in a reflectance value
171 over 0.6 in band 2 of the MOD09GA product and will, therefore, be identified as ice. However, the broadband albedo may
172 increase due to the thin snow layer. Further, low-albedo outcrops, cloud shadows, and meltwater ponding may decrease the
173 apparent ice albedo within one pixel.

174 3 Methods

175 First, we use two linear regression approaches to show baseline improvements to the ice albedo originally modeled by MAR.
176 Next, we use XGBoost to develop PIXAL, an optimized ice albedo model, and SHAP to elucidate the drivers of ice albedo.
177 The methods are described in more detail in Sect.3.1 to 3.3. We train the ice albedo models on cloud-free MODIS-derived ice
178 albedo observations since MODIS is not able to detect ice albedo conditions through clouds. For a fair comparison, we limit
179 our analysis to the co-located data points where cloud-free ice conditions are simultaneously modeled by MAR and observed
180 by MODIS. We evaluate the performance of the ice albedo models through a comparison with the test data set (the last 2 years
181 of the 2000-2021 period) of MODIS-derived ice albedo observations. We calculate the coefficient of determination (R^2) to
182 measure how well the models predict ice albedo compared to the MODIS observations. We also determine the mean squared
183 error (MSE) and mean absolute percentage error (MAPE) to measure the amount of error in the ice albedo models. The MAPE
184 provides a relative measure in percentages of the error of a prediction (de Myttenaere et al., 2016). Lastly, we calculate the
185 structural similarity index measure (SSIM). The SSIM is a performance metric from the field of computer vision developed to
186 determine the similarity between two images (Wang et al., 2004). The SSIM value we report in Sect. 4 is the mean of the SSIM
187 values between the daily images of the modeled and predicted ice albedo values from the test data set. The SSIM ranges
188 between -1 and 1, where 1 denotes a perfect similarity, -1 denotes perfect anti-similarity, and 0 indicates no similarity between
189 the two images. While we show in Sect. 4 that the XGBoost model shows optimal performance in modeling ice albedo, we
190 also tested a random forest (RF) and a high-performance symbolic regression (PySR), i.e. equation discovery. The RF is
191 described in Sect. 3.2. The PySR is a supervised ML model that aims to find an interpretable symbolic expression that optimizes
192 the simulation of a target variable (Cranmer, 2023). PySR uses a multi-population evolutionary algorithm, consisting of a
193 unique evolve-simplify-optimize loop designed to optimize unknown scalar constants in new empirical expressions. The
194 configurations for the RF and PySR are described in Appendix A.

195 3.1 Linear regression

196 The first baseline ice albedo model consists of updating the slope (0.05) and intercept (0.5) coefficients used in MAR by
197 training the original ice albedo equation (Eq. (1)) on the MODIS-derived ice albedo using linear regression. For the second
198 baseline ice albedo model, we create a linear regression of the form:

$$199 \alpha(x_1, \dots, x_n) = \beta_0 + \beta_1 x_1 + \dots + \beta_n x_n, \quad (2)$$



200 where x_1, \dots, x_n denote the MAR-based variables (or features) and β_0, \dots, β_n denote the coefficients. Again, we train the linear
201 regression on the MODIS-derived ice albedo. We use the seven MAR features that have the most impact on ice albedo: near-
202 surface temperature, runoff, shortwave downward radiation, meridional wind, surface height, surface slope, surface aspect.
203 The features are determined from the XGBoost and SHapley Additive exPlanations (SHAP) analyses, described in Sect. 3.2,
204 3.3, and 5.

205 3.2 XGBoost

206 Classic linear regression tools generally do not fully capture complex relationships between real-world properties, which are
207 often dynamic and nonlinear. We, therefore, employ the machine learning method XGBoost (Chen and Guestrin, 2016) to
208 learn the nonlinear relationships between observed ice albedo and the environmental drivers of ice albedo modeled by MAR.
209 XGBoost is an extension of the basic decision tree, a learning algorithm for classification and regression tasks. Decision trees
210 are supervised models that predict a target variable through simple threshold decisions on every variable in the input dataset.
211 Threshold decisions are made at each tree node, splitting the input data and the prediction of the target variable into two
212 branches that each connect to a threshold decision at the next node. Through each sequence of nodes and branches, a target
213 prediction can be made from a new set of input data. However, individual decision trees do not generalize data well and are
214 prone to overfitting. Averaging the target predictions of an ensemble of trees, such as in an RF architecture, can mitigate this
215 instability.

216 XGBoost is a scalable tree-boosting algorithm that uses a gradient descent algorithm to build an ensemble of parallel decision
217 trees based on subsets of the dataset (Chen and Guestrin, 2016). To minimize the prediction error, each decision tree in the
218 ensemble is built iteratively using targeted outcomes based on the gradient of the previous prediction error residuals. The final
219 prediction is the weighted average of the individual trees. XGBoost has seen successful applications in Earth and climate-
220 related studies in prediction (Fan et al., 2018; Huang et al., 2021; Ibrahim Ahmed Osman et al., 2021; Ma et al., 2020), image
221 classification (Colkesen and Ozturk, 2022; Nkiruka et al., 2021), reconstruction of remote sensing data gaps (Tan et al., 2021),
222 and risk assessment (Ma et al., 2021).

223 The predictor dataset consists of the MAR features (Sect. 2.1). We standardize the data to ensure no feature bias is present due
224 to different feature value ranges. We exclude albedo (AL2), cloud cover (CD, CM, and CU), and cloud optical depth (COD)
225 as input features because we include only cloud-free data points in both MAR and MODIS. To ensure snow, meltwater
226 ponding, cloud shadows, and outcrops erroneously identified as ice are not included in training the XGBoost, we constrain the
227 predictant albedo values from MODIS to be within the 2σ standard deviation range (0.165-0.671). We apply an 80-10-10
228 training-validation-testing split on our data stack, consisting of 5,384,250 data points spread over 22 years with 92 days in
229 each year and with 14 environmental features from MAR (described in Sect. 2.1). The test data set consists of the last two
230 years (2020 and 2021) of the data to avoid data leakage in the first years. We construct a regression tree ensemble with a
231 Pseudo-Huber loss function, which is less sensitive to outliers than the commonly used squared error loss (Huber, 1964). We
232 use an exact greedy tree construction algorithm for split finding to minimize the loss and a gmtree booster, which, each iteration,
233 builds the next tree and gives higher weights to misclassified points in the previous tree. We perform the hyper-parameter
234 search using Optuna (Akiba et al., 2019) and find the XGBoost configuration that yields optimal
235 performance using an MSE evaluation against the validation dataset. The configuration
236 includes a maximum tree depth (21), learning rate (0.07), number of boosted trees (500),
237 gamma ($2.38 \cdot 10^{-8}$), minimum child weight (10), subsample ratio (0.92), column subsample ratio (0.79), alpha (L1
238 regularization; 0.74), and lambda (L2 regularization; 0.33).



241 **3.3 Shapley additive explanations**

242 Machine learning models and their outcomes often lack interpretability, leading to complexities in their reliability assessment.
243 This challenge is addressed by a set of explainable AI tools and algorithms developed for understanding and interpreting ML
244 models that are regarded as inherently uninterpretable. We use SHAP (Lundberg and Lee, 2017), an explainable AI tool rooted
245 in the field of cooperative game theory, to explain and interpret our XGBoost model output and understand the roles of the
246 environmental properties, or features, in the input dataset in driving variability in ice albedo. The importance value of each
247 feature in the dataset, the SHAP value, is determined by iteratively training the XGBoost model on subsets of features. In each
248 iteration, a feature is systematically added or removed from the training dataset. The SHAP value of each feature is calculated
249 based on the difference in the predicted value between the model variations before and after adding or removing a feature. To
250 fully capture the additive SHAP value of all features, the model is trained on all possible feature subsets and a weighted average
251 of SHAP values for all model variations is determined. Positive SHAP values drive a positive change to the model prediction
252 with respect to the mean prediction and vice versa. Missing values have a zero SHAP value and, therefore, do not affect the
253 model prediction, making SHAP insensitive to data sparsity.
254

255 Significant successes have been made with SHAP in explaining machine learning models developed for the Earth and climate
256 studies related to classification (Descals et al., 2023; Temenos et al., 2023), predictions (Batunacun et al., 2021; Dikshit and
257 Pradhan, 2021; Ghafarian et al., 2022; Silva et al., 2022; Tang et al., 2022), and process understanding (Ishfaque et al., 2022).
258 Moreover, SHAP has seen uses in classifying Antarctic sea ice imagery (Koo et al., 2023), interpreting sea-level projections
259 (Rohmer et al., 2022), and studying the freeze-thaw cycle on the Tibetan plateau (Li et al., 2024). However, SHAP applications
260 in the cryosphere sciences are still limited. To our knowledge, this work is the first application of SHAP to ice albedo.

261 **4 Results**

262 MAR tends to have low performance in predicting ice albedo when evaluated against MODIS (Fig. 1; reds) with a low
263 coefficient of determination ($R^2 = 0.062$), mean squared error (MSE = 0.032), mean absolute percentage error (MAPE =
264 46.202%), and structural similarity index measure (SSIM = 0.112). The MAR albedo shows little variability with a mean of
265 0.56 ± 0.04 , an overestimation compared to the MODIS-derived ice albedo observations, which have a mean of 0.42 ± 0.11 .

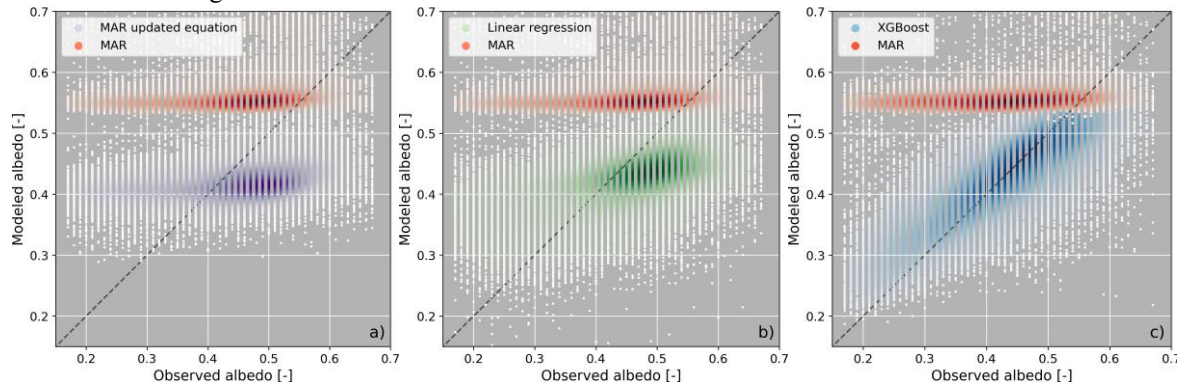
266 **4.1 Linear regression**

267 The two baseline linear regression approaches, described in Sect. 3.1, show an improvement over the ice albedo modeled with
268 MAR, with slightly better performance metrics when evaluated against the MODIS-derived ice albedo. The improved slope
269 (0.35) and intercept (0.20) compared to the MAR ice albedo equation (Eq. (1) and Sect. 2.1) result in a factor 2-3 improvement
270 of the $R^2 = 0.092$, MSE = 0.009 and MAPE = 22.385% (Fig. 1a; purples). However, a slight reduction is seen for the SSIM =
271 0.103. While the updated MAR equation provides a mean ice albedo of 0.42 ± 0.03 , similar to the mean MODIS-derived ice
272 albedo, it shows a too-low variability and generally underestimates the MODIS-observed ice albedo.
273

274 The ice albedo derived from the linear regression with runoff, surface slope, and the additional features mentioned in Sect. 3.1
275 shows a moderate improvement on the test set with regard to MAR, with $R^2 = 0.202$, MSE = 0.008, MAPE = 20.309%, and
276 SSIM = 0.285 (Fig. 1b; greens). Adding additional features beyond the seven most important ones did not achieve better
277 performance. The additional features we tested are: meltwater production (ME, mmWE/day), longwave downward radiation
278 (LWD, W/m²), surface atmospheric pressure (SP, hPa), ice density (RO1, kg/m³), liquid water content (WA1, kg/kg), snowfall



279 (SF, mmWE/day), and rainfall (RF, mmWE/day). The linear regression-derived ice albedo has a mean of 0.42 ± 0.05 but still
280 generally underestimates the MODIS-derived ice albedo. The spread in the linear regression-derived albedo values is larger
281 than for MAR and the updated MAR equation. However, the large variability seen in the MODIS-derived ice albedo is not
282 achieved with the linear regression.



283 **Figure 1: Scatter plot for JJA in 2020-2021 between MODIS-derived ice albedo (x-axis) and ice albedo modeled with MAR (a,b,c;**
284 **red) and ice albedo modeled with a) the updated slope and intercept coefficients of the MAR ice albedo equation (Eq. (1)) (purple),**
285 **b) linear regression with additional features (green), c) and XGBoost (blue). The dashed line represents the 1:1 line.**

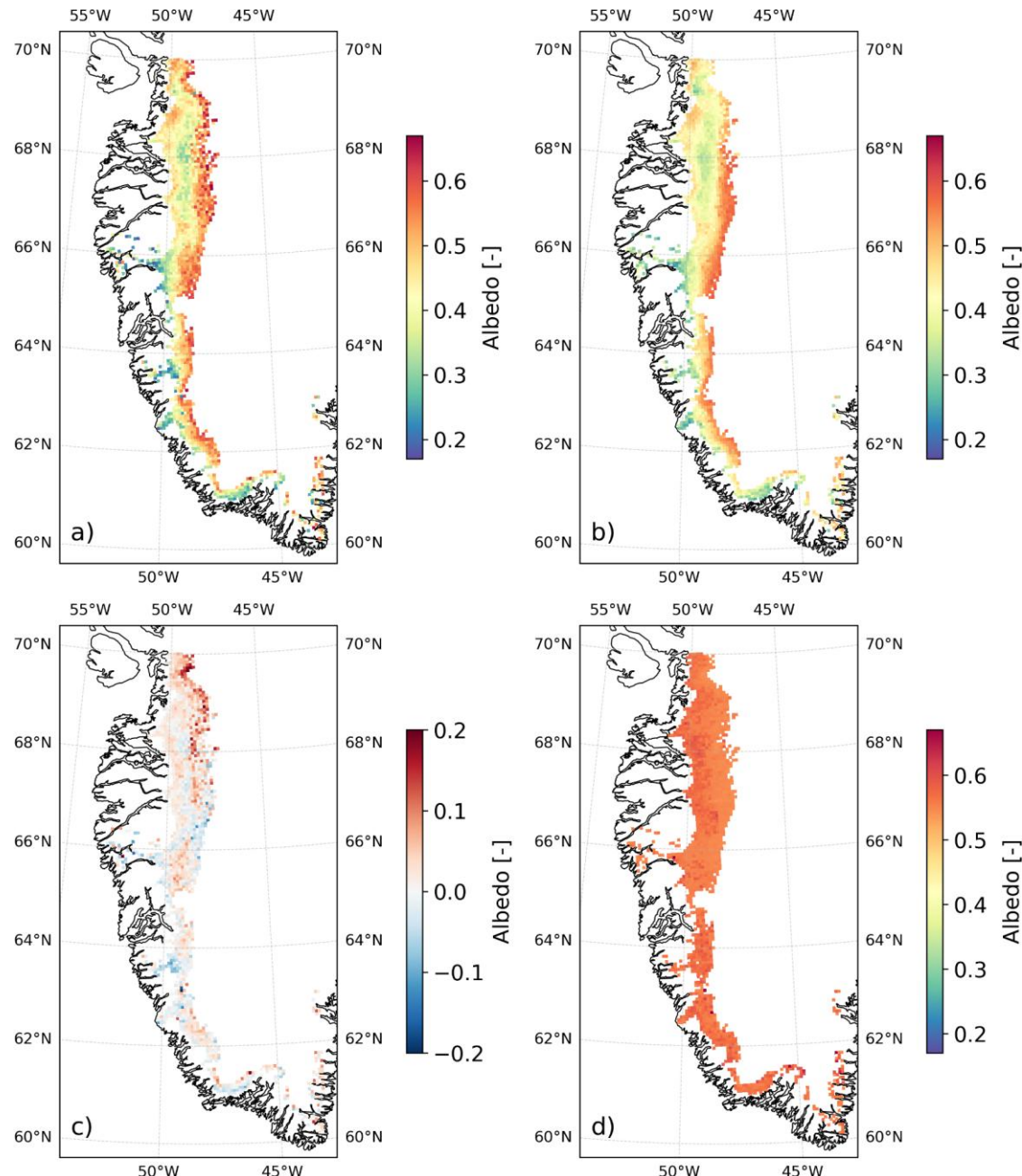
287

288 4.2 XGBoost

289 The ice albedo modeled with XGBoost shows major improvements on the test set in all performance metrics with $R^2 = 0.568$,
290 $MSE = 0.005$, $MAPE = 14.646\%$, and $SSIM = 0.624$. The XGBoost-modeled ice albedo has a mean of 0.42 ± 0.08 , and exhibits
291 a variability similar to the MODIS-derived ice albedo. XGBoost represents ice albedo values between 0.4 and 0.6 well but
292 slightly overestimates low-albedo values (Fig. 1c; blues).

293

294 Figure 2a shows the mean MODIS-derived ice albedo for JJA in 2020-2021. The ice albedo modeled by XGBoost (Fig. 2b)
295 below 66°N shows a similar decreasing pattern in ice albedo from the snowline to the ice sheet margin as observed with
296 MODIS. Above 66°N , the XGBoost-modeled ice albedo exhibits a bimodal distribution, similar to MODIS, with high values
297 near the ice margin and near the snow line. Low albedo values are found in between the margin and snow line, which represent
298 the dark ice zone. Compared to the MODIS-derived ice albedo, the XGBoost slightly underestimates albedo at the snowline
299 near Jakobshavn Glacier at $69\text{--}70^{\circ}\text{N}$ and slightly overestimates albedo in some areas near the ice margin in the central and
300 southern regions (Fig. 2c). Generally, the XGBoost provides a higher spatial ice albedo variability across the study area than
301 MAR (Fig. 2d).



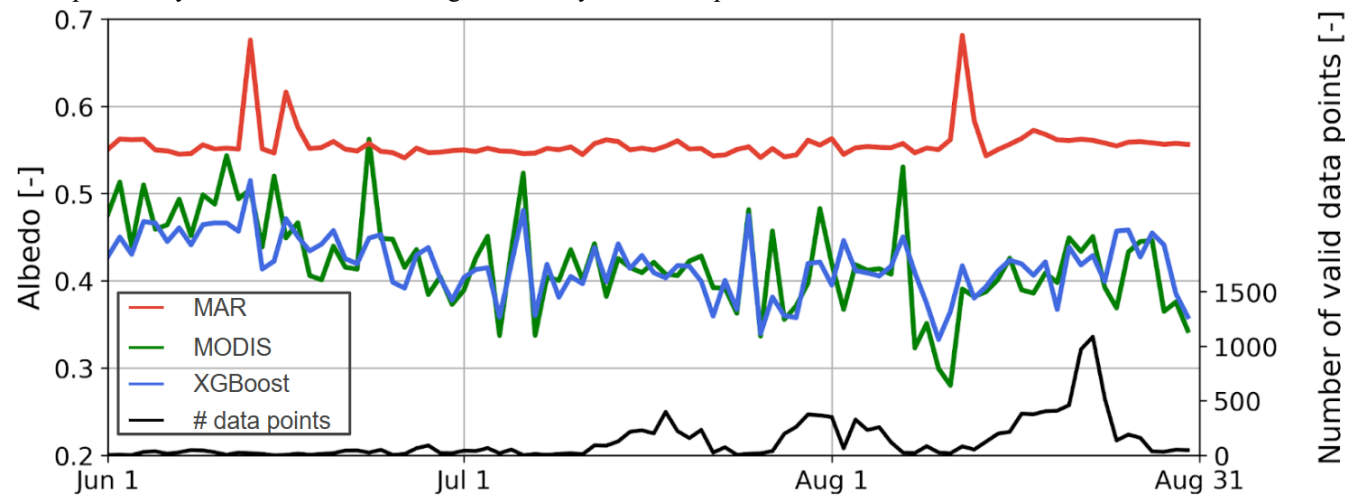
302
303

Figure 2: Mean ice albedo for JJA in 2020-2021 for a) MODIS, b) XGBoost, c) difference MODIS-XGBoost, and d) MAR.

304
305
306
307
308

Additionally, XGBoost provides considerable improvements in temporal ice albedo modeling compared to the ice albedo from MAR. Figure 3 shows the ice albedo during JJA averaged over 2020 and 2021. XGBoost (Fig. 3; blue line) shows close daily alignment with the MODIS-derived ice albedos (Fig. 3: green line) throughout the melting season. Especially in July and August, when larger ice areas are exposed compared to earlier in the melting season (Fig. 3; black line) (Antwerpen et al.,

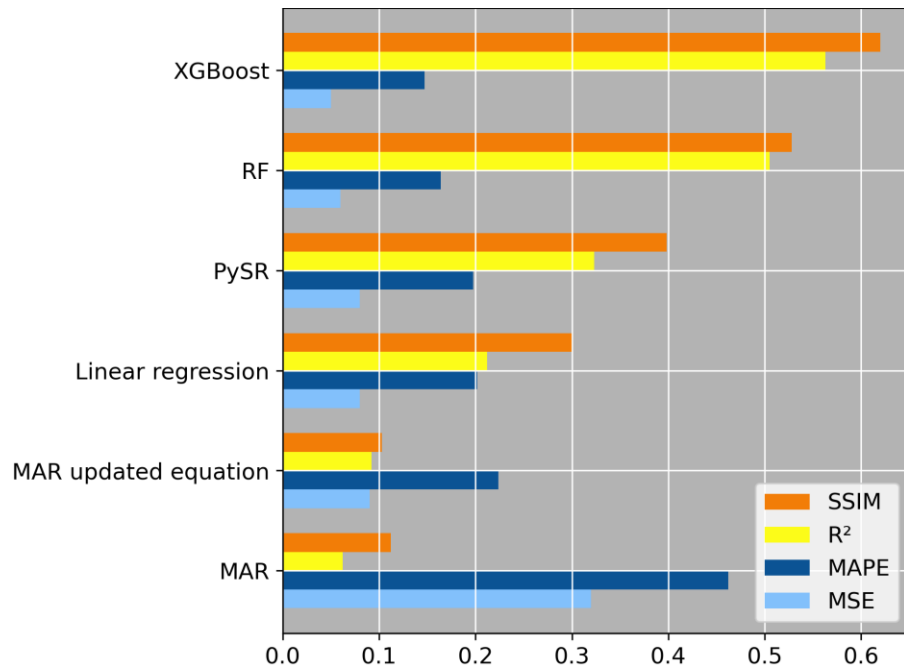
309 2022; Noël et al., 2019). In the first half of June, when ice exposure is low, XGBoost slightly underestimates the MODIS-
310 derived ice albedo while still outperforming MAR (Fig. 3; red line). Generally, XGBoost slightly underestimates high-albedo
311 values and slightly overestimates low-albedo values. The peak albedo values (> 0.6) from MAR represent data points with
312 fresh snow or firn cover that have been misidentified as ice. Anomalously high albedo values can occur, especially during low
313 ice exposure days, due to a skewed average when only a few data points are available.



314
315 **Figure 3: Daily mean ice albedo across the southwestern GrIS for JJA averaged over 2020 and 2021 (test set) for MAR (red), MODIS**
316 **(green), and XGBoost (blue). The black line indicates the mean number of ice albedo data points per day.**

318 4.3 Model performance evaluation

319 The performance metrics of all our ice albedo model configurations evaluated against the MODIS-derived ice albedo
320 observations are shown in Fig. 4. The correlations between the ice albedo modeled with RF and with PySR and the ice albedo
321 observed with MODIS are shown in Figs. A1 and A2. The ML architectures (XGBoost, RF, and PySR) perform considerably
322 better than the non-ML architectures (MAR, updated MAR equation, and linear regression), showcasing the superiority of ML
323 in modeling ice albedo. While the symbolic regression method used in the PySR architecture can provide explicit insights into
324 the developed ice albedo model, it shows a considerably lower performance than the XGBoost. We, therefore, do not use the
325 symbolic regression insights from PySR in this study as they still have low predictive power. The RF architecture shows
326 considerable improvement over MAR. However, the XGBoost model shows optimal performance with the highest R^2 and
327 SSIM scores and the lowest MSE and MAPE scores.

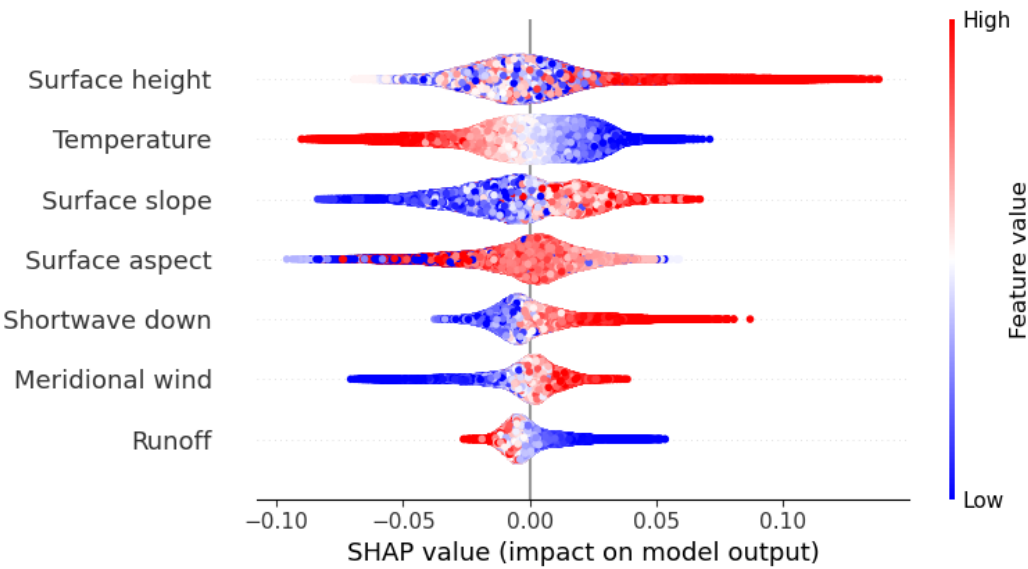


328
329 **Figure 4: Performance metrics of ice albedo models vs MODIS-derived albedo. For visualization purposes, MSE is multiplied by 10**
330 **and MAPE is divided by 100. For MSE and MAPE, lower scores represent a better performance. For R² and SSIM, higher scores**
331 **represent a better performance.**

332

333 4.4 SHAP analysis

334 Our PIXAL algorithm includes two parts: a predictive model, based on XGBoost, and an explainable AI component to reveal
335 the drivers of ice albedo that can be used to gain insights into potential MAR model improvement. The SHAP values of the
336 seven most important MAR-based features are listed in Fig. 5. The importance of each feature in controlling ice albedo is
337 determined by the magnitude of its impact on the final ice albedo prediction from XGBoost (SHAP value), with respect to the
338 mean ice albedo prediction (0.42). In other words, the SHAP value shows how much the ice albedo prediction increases or
339 decreases due to each individual feature relative to the mean ice albedo. The features are ordered by the mean absolute SHAP
340 values, which emphasizes the average impact and gives less weight to high-magnitude SHAP values. The topographic features
341 of surface height and slope are primary drivers of ice albedo and environmental, radiative, and atmospheric features are
342 secondary drivers.



343
344 **Figure 5: SHAP values for the seven most important MAR features.** The SHAP value represents the impact a feature has on the ice
345 albedo prediction, relative to the mean ice albedo prediction. A feature with a positive SHAP value indicates that the feature increases
346 the ice albedo prediction and vice versa. The features are sorted by their mean absolute SHAP values in ascending order. Red
347 indicates high feature values and blue indicates low feature values.

348

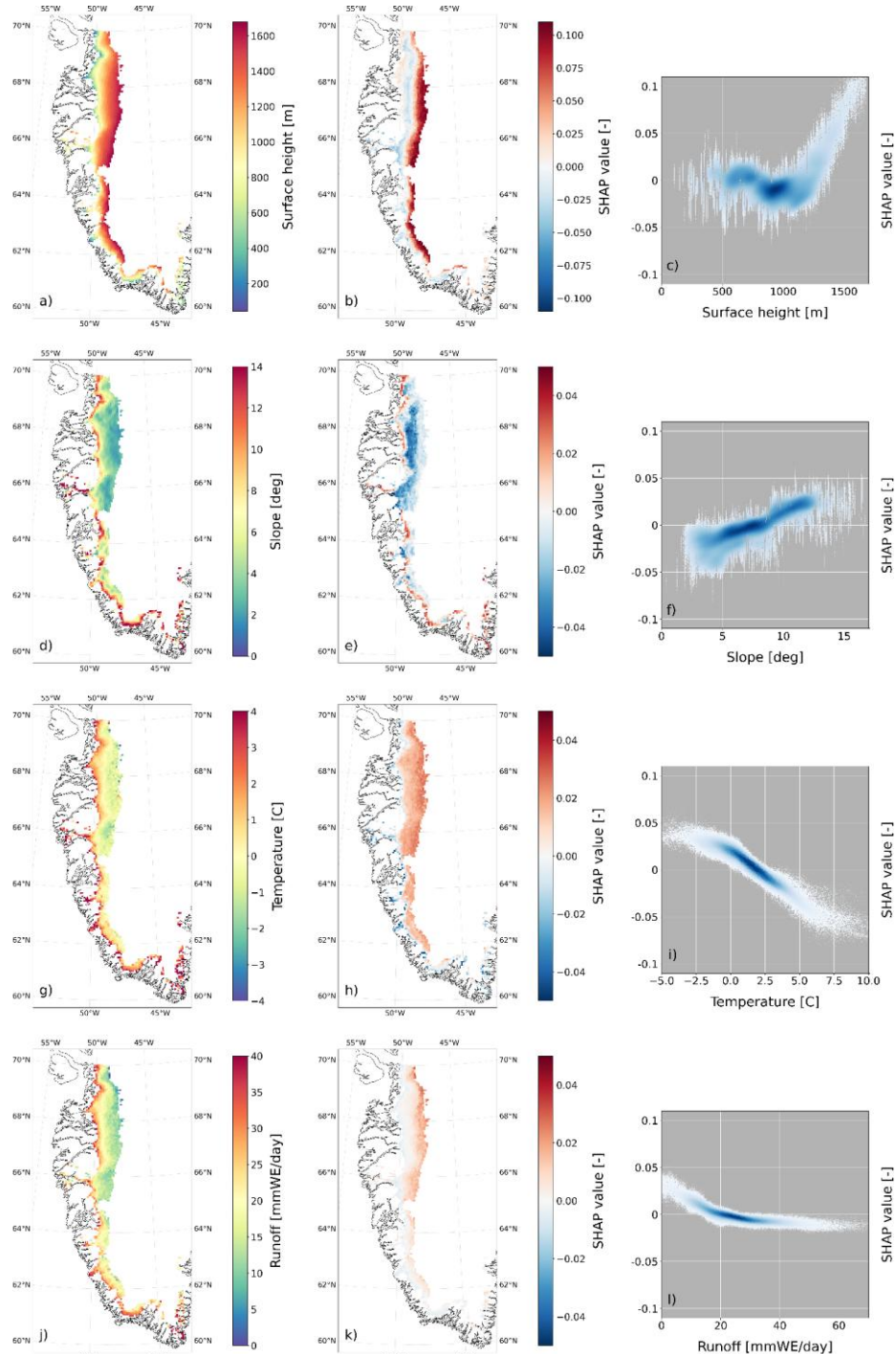
349 **5 Discussion**

350 **5.1 Drivers of ice albedo**

351 Surface height exhibits a nonlinear relationship with its SHAP values (Fig. 6a-c). The SHAP values show the strong impact of
352 surface height on albedo, ranging from -0.05 to 0.1, with the lowest albedo values present at low elevations near the ice margin
353 and high albedo values present at high elevations near the snow line. These findings are in line with previous studies on ice
354 albedo drivers (Feng et al., 2024; Moustafa et al., 2015). As the melting season commences and temperatures rise, snowmelt
355 first occurs at the ice margin, exposing the underlying ice. The snowline then retreats to higher elevations, resulting in lower-
356 elevation ice experiencing longer exposure. Longer ice exposure can result in a lower albedo as it allows for more accumulation
357 of LACs from local and distant sources. Algal blooms are also given more time to grow and spread if uninterrupted by snowfall
358 events. Snowmelt events at higher elevations may add to the LAC concentrations at lower elevations when meltwater is
359 transported toward the ice margin and LACs may remain behind on the ice surface. Higher ice sheet elevations are generally
360 further from local LAC sources, such as moraines, dunes, dry proglacial floodplains, ground transport, and industry, reducing
361 the potential for LAC deposition. Furthermore, englacial Holocene dust mostly melts out at lower elevations due to the flow
362 configuration of the GrIS, adding to the LAC concentration and albedo darkening at low elevations (MacGregor et al., 2020;
363 Wientjes et al., 2012). A large low-albedo region is present at ~800-1100 m a.s.l. above 66 °N, representing the dark ice zone
364 where the highest concentrations of LACs are found (Shimada et al., 2016; Wang et al., 2020). Moreover, at low elevations,
365 older, denser ice is exposed, which has fewer and smaller englacial air bubbles, reducing the albedo.
366



367 Conversely, longer ice exposure can cause an increase in albedo. Ice erodes as it is exposed to the environment in strong
368 incoming shortwave radiation conditions, affecting the metamorphic state and creating a porous weathering crust with a low
369 density (Munro, 1990). During conditions with low amounts of meltwater, a weathering crust has many interfaces between the
370 ice and air, allowing for light scattering with a high angle, which increases albedo (Jonsell et al., 2003). The relationship
371 between albedo and surface height will likely change in the future with increasing temperatures, expanding the melting season
372 and causing earlier ice exposure, as well as later snow-covering. Therefore, ice is exposed for longer periods, potentially
373 exacerbating the processes related to ice metamorphism and LAC accumulation, lowering the albedo. These processes will
374 also occur more frequently and for longer periods at higher elevations as the snowline rises with increasing temperature.



375
 376 **Figure 6: Feature values, SHAP values (impact of feature values on ice albedo), and the feature and SHAP value correlation for**
 377 **surface height (a-c), slope (d-f), near-surface air temperature (g-i), and runoff (j-l). The maps show the average over JJA in 2020-**
 378 **2021. Note the larger range of SHAP values for surface height in b, compared to the SHAP value range used in e, h, and k.**



379

380 The surface slope and its SHAP values have a linear and positive relationship, with SHAP values ranging between -0.05 and
381 0.05 (Fig. 6d-f). A flat ice surface, typically found at higher elevations and the dark ice zone, correlates to low albedo values.
382 Higher albedo values are found on steeper ice surface slopes at the ice margin. This relationship likely represents the potential
383 for meltwater and LACs to accumulate more efficiently on flat ice surfaces (Wientjes and Oerlemans, 2010; Zuo and
384 Oerlemans, 1996). The positive relationship between surface slope and albedo is at odds with the results from Feng et al.
385 (2024), who find that darker ice is found on steeper ice slopes. However, this relationship mostly holds for the southeastern
386 GrIS while the link between slope and albedo is less strong for the southwestern GrIS.

387

388 While surface aspect is shown as an important driver of ice albedo in Fig. 5, this is due to the large impact of a few extreme
389 feature values on ice albedo (Fig. A3). The common west-facing aspect angle (250-300°) does not affect ice albedo much on
390 the southwestern GrIS (Fig. A3c). Some of the southwest-facing ice surfaces (300-360°) show a lower albedo, potentially due
391 to increased algal bloom activity in response to increased solar radiation. However, we find no significant relationship between
392 shortwave downward radiation and ice albedo or aspect (Fig. A4). Additionally, the 6.5 km resolution is likely not sufficient
393 to represent the spatial variability of the aspect and its effects on ice albedo.

394

395 The topographic features in MAR do not change with time. Potential changes in the relationships between topographic features
396 and ice albedo may, therefore, not be fully captured by MAR. Nonetheless, during the early Holocene (~12-7 ka), the most
397 recent period with warmer-than-present temperatures in Greenland (Badgeley et al., 2020), maximum ice margin retreat rates
398 of the southwestern GrIS were ~35 m/y (Briner et al., 2020). Assuming similar present-day retreat rates, the estimate of ice
399 margin retreat at the end of this century would be ~2,660 m, which only constitutes ~40% of one 6.5 km grid cell in MAR.
400 We, therefore, assume that the physical configuration of the GrIS will not change significantly by 2100 and that the static
401 topographic features in MAR are sufficiently accurate for the purposes of this study.

402

403 There is a strong negative linear relationship (-0.009/°C; $R^2 = 0.884$) between near-surface air temperature and its SHAP values
404 (Fig. 6g-i). High temperatures are generally found at the ice sheet margin, while low temperatures are found at higher
405 elevations. Temperatures below 0 °C can cause refreezing of meltwater in the shallow subsurface ice layers and superficial
406 meltwater ponds and streams, increasing the albedo. Conversely, temperatures above 0 °C can cause thin, freshly fallen snow
407 layers to melt and expose the lower-albedo ice underneath. High temperatures generally promote biological growth of algal
408 blooms (Uetake et al., 2010), decreasing the albedo. Moreover, high temperatures are mostly found near the ice margin, where
409 there is closer proximity to local LAC sources and, thus, a higher likelihood of LAC deposition, including bioavailable
410 nutrients, which further promotes algae growth.

411

412 Runoff has a strong negative near-linear relationship with ice albedo, for SHAP values for runoff below ~25 mmWE/day,
413 which can be partly explained by the dependence of runoff on near-surface temperature. In this range, runoff promotes ice
414 albedo decrease through the accumulation of meltwater in ponds and streams and by filling up shallow microcavities in the
415 upper ice layers. Runoff and decreasing ice albedo are further enhanced by the positive meltwater-albedo feedback. At runoff
416 values of ~25 mmWE/day, maximum albedo reduction is achieved and almost no further ice albedo decrease is observed (Fig.
417 6l). The cutoff of 25 mmWE/day may signify a saturated ice surface and sub-surface where no more meltwater can be retained,
418 causing any additional meltwater to run off to lower elevations. Moreover, increased runoff and meltwater production on the
419 upper ice layers can cause increased melt-out of englacial Holocene dust and the development of cryoconite holes, further
420 lowering the albedo.

421



422 The additional features listed in Fig. 5 are shown as important features because they are ordered by their absolute mean SHAP
423 values, which gives more weight to the average impact of the feature and de-emphasizes high-impact SHAP values. However,
424 these features do not show a high impact on ice albedo and are, therefore, not discussed here.

425 5.2 Limitations

426 Some MAR features can be biased due to potential dependencies on the inaccurately modeled ice albedo in MAR. This bias
427 could be propagated to the PIXAL output. A solution to reduce this bias would be an iterative approach of embedding PIXAL
428 in MAR, rerunning MAR, and updating PIXAL with the updated MAR output. This process can be repeated until a desired
429 accuracy and error reduction is achieved. However, this method is outside the scope of this paper and we hope to apply it in a
430 future publication.

431 Our results reveal relationships between ice albedo and environmental ice sheet conditions. Several of these drivers may
432 account for some processes related to LAC-driven ice sheet darkening. However, PIXAL is trained on the available
433 topographic, atmospheric, radiative, and glaciologic features in MAR and can, thus, only learn physical processes that can be
434 inferred from these features. Additionally, other physical processes may not be fully captured by PIXAL, including the
435 biological activity of algae, deposition of black carbon, dust, and ash released by deserts, local dried-up flood plains, forest
436 fires, volcanic eruptions, anthropogenic emissions, and the melt-out of englacial Holocene dust. Positive feedback systems
437 related to LACs, which could accelerate ice albedo darkening, may, therefore, also be missed.

439
440 Moreover, we use modeled estimates of the environmental features which poses limitations to the trustworthiness of the derived
441 results. While MAR is a state-of-the-art regional climate model that has been validated over the GrIS (Fettweis et al., 2017),
442 it still exhibits some biases, especially on albedo. Similarly, while MODIS has outstanding capabilities in measuring albedo,
443 it has limitations related to atmospheric corrections, a fundamental reflectance data processing step. To account for radiance,
444 reflectance, and transmittance effects due to atmospheric aerosol loading, a radiative transfer model is applied (Vermote et al.,
445 2002). However, a per-pixel analysis of MODIS observations is infeasible due to computational costs (Vermote et al., 1997).
446 Therefore, a simplified approach is applied using a look-up table for different aerosol loadings and sun-view geometries,
447 potentially leading to inaccurate corrections. Moreover, NASA's Terra 10:30 AM overpass time could incur a bias towards
448 higher albedo measurements because the darkening effect of meltwater production will occur mostly in strong incoming
449 radiation and high-temperature conditions during the afternoon. The relationships we find between the MAR features and the
450 MODIS-derived ice albedo might, therefore, in part arise from model imperfections and measurement biases.

451
452 While we train PIXAL only on the southwestern GrIS ice albedo, many physical processes are generalizable and hold in other
453 glaciated areas, e.g., the relationship between temperature, ice melting, and ice albedo change. However, some processes may
454 be specific to the southwestern GrIS, such as the dependency of ice albedo on surface height, slope, and aspect. Moreover,
455 processes relating to LAC deposition are likely specific to the southwestern GrIS as these are dependent on the LAC source
456 location, atmospheric circulation patterns for transport, and topographical characteristics of the ice.

457
458 PIXAL is intended for both hindcasting and forecasting purposes. Because of the unknown effects of climate change on the
459 environmental conditions on and near Greenland, a changing distribution of environmental feature values is expected for the
460 rest of the century, e.g. more frequent high temperatures. Out-of-distribution values for input features generally pose a problem
461 for the stability of ML models. However, the current spread of values in our large dataset ($\sim 6\sigma$) accounts for most of the
462 expected extreme values. While these extreme values may become more common toward the end of the century, PIXAL is
463 trained on and familiar with these values. We, therefore, do not expect significant issues relating to out-of-distribution values



464 in forecasts. Except for surface height, with ice exposure likely occurring at higher and unprecedented elevations with
465 continued atmospheric warming during the rest of the century.

466 **6 Conclusions**

467 We explored a suite of linear and nonlinear regression architectures to develop PIXAL and improve ice albedo estimates on
468 the southwestern Greenland ice sheet. Our findings highlight XGBoost as the best-performing architecture, which outperforms
469 a state-of-the-art regional climate model, MAR, in modeling ice albedo. The performance metrics as evaluated against the
470 MODIS-derived ice albedo observations improved substantially compared to MAR with an increased R^2 from 0.062 to 0.563,
471 an increased SSIM from 0.112 to 0.620, a decreased MSE from 0.032 to 0.005, and a decreased MAPE from 46.202% to
472 14.699%. We find that the most important drivers of ice albedo are the topographic features, specifically the ice sheet surface
473 height and slope. Surface height has a nonlinear impact on albedo, but low albedo values are generally found at lower
474 elevations, likely due to the longer ice exposure which induces increased accumulation of LACs, melting out of englacial
475 Holocene dust, and algal bloom activity. The ice at lower elevations is generally older and denser and has fewer and smaller
476 englacial air bubbles, further reducing the albedo. We find low ice albedo values on flat ice surfaces where meltwater and
477 LACs are more likely to accumulate. A steep ice surface less efficiently retains meltwater and LACs and, therefore, has a
478 higher potential for increased albedo. Additionally, we found that near-surface air temperature and runoff as strong drivers of
479 ice albedo. Temperatures below 0 °C can increase ice albedo by refreezing meltwater, while temperatures above 0 °C can
480 decrease ice albedo by melting thin snow layers and promoting algal bloom activity. Runoff can cause a decrease in ice albedo
481 up to runoff values of ~25 mmWE/day. Above this threshold, the upper ice layers are likely saturated with meltwater and the
482 albedo does not decrease further. An explicit understanding of the emission, transport, and deposition of LACs onto the GrIS
483 and other glaciated areas is essential for further improvements to PIXAL and general ice albedo modeling. PIXAL paves the
484 way for a new generation of climate models that are more adept at modeling ice albedo and ice sheet melting. This work
485 provides a significant step forward in ice sheet modeling for Earth system models and provides new insights on ice albedo and
486 its drivers, the short and long-term future of the GrIS, and global and local sea level change.
487



488 **Code availability**

489 The MAR code and output are available from <ftp://ftp.climate.be/fettweis/MARv3.12>. The code used to analyze the model and
490 satellite data is available upon request from the corresponding author

491 **Data availability**

492 All data needed to evaluate the conclusions in the paper are present in the paper. Additional data related to this paper may be
493 requested from the authors. The MODIS MOD10A1 and MOD09GA data are available at:
494 https://developers.google.com/earth-engine/datasets/catalog/MODIS_061_MOD10A1 and
495 https://developers.google.com/earth-engine/datasets/catalog/MODIS_061_MOD09GA.

496 **Author contribution**

497 Conceptualization: RA, MT, PG. Methodology: RA, MT, PG, XF, WJB. Investigation: RA. Visualization: RA. Supervision:
498 MT, PG. Writing - original draft: RA. Writing - review & editing: MT, PG, XF, WJB. Funding acquisition: MT, PG.

499 **Competing interests**

500 At least one of the (co-)authors is a member of the editorial board of The Cryosphere.

501 **Financial support**

502 This research has been supported by the National Science Foundation (NSF) (award #OPP-2136938), NSF Science
503 and Technology Center (STC) Learning the Earth With Artificial Intelligence and Physics (LEAP) (award
504 #2019625), Heising-Simons Foundation (award #1029-1160), and NASA GISS (award #16426).
505



506 **References**

507 Akiba, T., Sano, S., Yanase, T., Ohta, T., Koyama, M., 2019. Optuna: A Next-generation Hyperparameter Optimization
508 Framework. <https://doi.org/10.48550/arXiv.1907.10902>

509 Alexander, P.M., Tedesco, M., Fettweis, X., van de Wal, R.S.W., Smeets, C.J.P.P., van den Broeke, M.R., 2014. Assessing
510 spatio-temporal variability and trends in modelled and measured Greenland Ice Sheet albedo (2000–2013). *The
511 Cryosphere* 8, 2293–2312. <https://doi.org/10.5194/tc-8-2293-2014>

512 Amino, T., Iizuka, Y., Matoba, S., Shimada, R., Oshima, N., Suzuki, T., Ando, T., Aoki, T., Fujita, K., 2021. Increasing dust
513 emission from ice free terrain in southeastern Greenland since 2000. *Polar Sci.* 27, 100599.
514 <https://doi.org/10.1016/j.polar.2020.100599>

515 Antwerpen, R.M., Tedesco, M., Fettweis, X., Alexander, P., van de Berg, W.J., 2022. Assessing bare-ice albedo simulated
516 by MAR over the Greenland ice sheet (2000–2021) and implications for meltwater production estimates. *The Cryosphere*
517 16, 4185–4199. <https://doi.org/10.5194/tc-16-4185-2022>

518 Aschwanden, A., Fahnestock, M.A., Truffer, M., Brinkerhoff, D.J., Hock, R., Khroulev, C., Mottram, R., Khan, S.A., 2019.
519 Contribution of the Greenland Ice Sheet to sea level over the next millennium. *Sci. Adv.* 5, eaav9396.
520 <https://doi.org/10.1126/sciadv.aav9396>

521 Badgeley, J.A., Steig, E.J., Hakim, G.J., Fudge, T.J., 2020. Greenland temperature and precipitation over the last 20 000
522 years using data assimilation. *Clim. Past* 16, 1325–1346. <https://doi.org/10.5194/cp-16-1325-2020>

523 Batunacun, Wieland, R., Lakes, T., Nendel, C., 2021. Using Shapley additive explanations to interpret extreme gradient
524 boosting predictions of grassland degradation in Xilingol, China. *Geosci. Model Dev.* 14, 1493–1510.
525 <https://doi.org/10.5194/gmd-14-1493-2021>

526 Bond, T.C., Doherty, S.J., Fahey, D.W., Forster, P.M., Berntsen, T., DeAngelo, B.J., Flanner, M.G., Ghan, S., Kärcher, B.,
527 Koch, D., Kinne, S., Kondo, Y., Quinn, P.K., Sarofim, M.C., Schultz, M.G., Schulz, M., Venkataraman, C., Zhang, H.,
528 Zhang, S., Bellouin, N., Guttikunda, S.K., Hopke, P.K., Jacobson, M.Z., Kaiser, J.W., Klimont, Z., Lohmann, U.,
529 Schwarz, J.P., Shindell, D., Storelvmo, T., Warren, S.G., Zender, C.S., 2013. Bounding the role of black carbon in the
530 climate system: A scientific assessment. *J. Geophys. Res. Atmospheres* 118, 5380–5552.
531 <https://doi.org/10.1002/jgrd.50171>

532 Briner, J.P., Cuzzone, J.K., Badgeley, J.A., Young, N.E., Steig, E.J., Morlighem, M., Schlegel, N.-J., Hakim, G.J., Schaefer,
533 J.M., Johnson, J.V., Lesnek, A.J., Thomas, E.K., Allan, E., Bennike, O., Cluett, A.A., Csatho, B., de Vernal, A., Downs,
534 J., Larour, E., Nowicki, S., 2020. Rate of mass loss from the Greenland Ice Sheet will exceed Holocene values this
535 century. *Nature* 586, 70–74. <https://doi.org/10.1038/s41586-020-2742-6>

536 Brun, E., David, P., Sudul, M., Brunot, G., 1992. A numerical model to simulate snow-cover stratigraphy for operational
537 avalanche forecasting. *J. Glaciol.* 38, 13–22. <https://doi.org/10.3189/S0022143000009552>

538 Cali Quaglia, F., Meloni, D., Muscari, G., Di Iorio, T., Ciardini, V., Pace, G., Becagli, S., Di Bernardino, A., Cacciani, M.,
539 Hannigan, J.W., Ortega, I., di Sarra, A.G., 2022. On the Radiative Impact of Biomass-Burning Aerosols in the Arctic:
540 The August 2017 Case Study. *Remote Sens.* 14, 313. <https://doi.org/10.3390/rs14020313>

541 Cathles L.M., Abbot D.S., Bassis J.N., MacAyeal D.R. Modeling surface-roughness/solar-ablation feedback: application to
542 small-scale surface channels and crevasses of the Greenland ice sheet. *Annals of Glaciology.* 2011;52(59):99-108.
543 doi:10.3189/172756411799096268

544

545 Chen, T., Guestrin, C., 2016. XGBoost: A Scalable Tree Boosting System, in: Proceedings of the 22nd ACM SIGKDD
546 International Conference on Knowledge Discovery and Data Mining. pp. 785–794.
547 <https://doi.org/10.1145/2939672.2939785>

548 Colkesen, I., Ozturk, M.Y., 2022. A comparative evaluation of state-of-the-art ensemble learning algorithms for land cover



549 classification using WorldView-2, Sentinel-2 and ROSIS imagery. *Arab. J. Geosci.* 15, 942.
550 <https://doi.org/10.1007/s12517-022-10243-x>

551 Cook, J.M., Tedstone, A.J., Williamson, C., McCutcheon, J., Hodson, A.J., Dayal, A., Skiles, M., Hofer, S., Bryant, R.,
552 McAre, O., McGonigle, A., Ryan, J., Anesio, A.M., Irvine-Fynn, T.D.L., Hubbard, A., Hanna, E., Flanner, M.,
553 Mayanna, S., Benning, L.G., van As, D., Yallop, M., McQuaid, J.B., Gribbin, T., Tranter, M., 2020. Glacier algae
554 accelerate melt rates on the south-western Greenland Ice Sheet. *The Cryosphere* 14, 309–330. <https://doi.org/10.5194/tc-14-309-2020>

555 Cranmer, M., 2023. Interpretable Machine Learning for Science with PySR and SymbolicRegression.jl.
556 <https://doi.org/10.48550/ARXIV.2305.01582>

557 de Myttenaere, A., Golden, B., Le Grand, B., Rossi, F., 2016. Mean Absolute Percentage Error for regression models.
558 *Neurocomputing, Advances in artificial neural networks, machine learning and computational intelligence* 192, 38–48.
559 <https://doi.org/10.1016/j.neucom.2015.12.114>

560 Descals, A., Verger, A., Yin, G., Filella, I., Peñuelas, J., 2023. Local interpretation of machine learning models in remote
561 sensing with SHAP: the case of global climate constraints on photosynthesis phenology. *Int. J. Remote Sens.* 44, 3160–
562 3173. <https://doi.org/10.1080/01431161.2023.2217982>

563 Dikshit, A., Pradhan, B., 2021. Interpretable and explainable AI (XAI) model for spatial drought prediction. *Sci. Total
564 Environ.* 801, 149797. <https://doi.org/10.1016/j.scitotenv.2021.149797>

565 Evangeliou, N., Kylling, A., Eckhardt, S., Myroniuk, V., Stebel, K., Paugam, R., Zibtsev, S., Stohl, A., 2019. Open fires in
566 Greenland in summer 2017: transport, deposition and radiative effects of BC, OC and BrC emissions. *Atmospheric
567 Chem. Phys.* 19, 1393–1411. <https://doi.org/10.5194/acp-19-1393-2019>

568 Fan, J., Wang, X., Wu, L., Zhou, H., Zhang, F., Yu, X., Lu, X., Xiang, Y., 2018. Comparison of Support Vector Machine
569 and Extreme Gradient Boosting for predicting daily global solar radiation using temperature and precipitation in humid
570 subtropical climates: A case study in China. *Energy Convers. Manag.* 164, 102–111.
571 <https://doi.org/10.1016/j.enconman.2018.02.087>

572 Feng, S., Cook, J.M., Naegeli, K., Anesio, A.M., Benning, L.G., Tranter, M., 2024. The Impact of Bare Ice Duration and
573 Geo-Topographical Factors on the Darkening of the Greenland Ice Sheet. *Geophys. Res. Lett.* 51, e2023GL104894.
574 <https://doi.org/10.1029/2023GL104894>

575 Fettweis, X., Box, J.E., Agosta, C., Amory, C., Kittel, C., Lang, C., van As, D., Machguth, H., Gallée, H., 2017.
576 Reconstructions of the 1900–2015 Greenland ice sheet surface mass balance using the regional climate MAR model. *The
577 Cryosphere* 11, 1015–1033. <https://doi.org/10.5194/tc-11-1015-2017>

578 Fettweis, X., Hofer, S., Séférian, R., Amory, C., Delhasse, A., Doutreloup, S., Kittel, C., Lang, C., Van Bever, J., Veillon, F.,
579 Irvine, P., 2021. Brief communication: Reduction in the future Greenland ice sheet surface melt with the help of solar
580 geoengineering. *The Cryosphere* 15, 3013–3019. <https://doi.org/10.5194/tc-15-3013-2021>

581 Flanner, M.G., Arnheim, J.B., Cook, J.M., Dang, C., He, C., Huang, X., Singh, D., Skiles, S.M., Whicker, C.A., Zender,
582 C.S., 2021. SNICAR-ADv3: a community tool for modeling spectral snow albedo. *Geosci. Model Dev.* 14, 7673–7704.
583 <https://doi.org/10.5194/gmd-14-7673-2021>

584 Flanner, M.G., Zender, C.S., 2006. Linking snowpack microphysics and albedo evolution. *J. Geophys. Res.* 111, D12208.
585 <https://doi.org/10.1029/2005JD006834>

586 Fox-Kemper, B., Hewitt, H.T., Xiao, C., Aðalgeirs Þóttir, G., Drijfhout, S.S., Edwards, T.L., Golledge, N.R., Hemer, M.,
587 Kopp, R.E., Krinner, G., Mix, A., Notz, D., Nowicki, S., Nurhati, I.S., Ruiz, L., Sallée, J.-B., Slangen, A.B.A., Yu, Y.,
588 2021. Ocean, cryosphere, and sea level change, in: Masson-Delmotte, V., Zhai, P., Pirani, A., Connors, S.L., Péan, C.,
589 Berger, S., Caud, N., Chen, Y., Goldfarb, L., Gomis, M.I., Huang, M., Leitzell, K., Lonnoy, E., Matthews, J.B.R.,
590 Maycock, T.K., Waterfield, T., Yelekçi, Ö., Yu, R., Zhou, B. (Eds.), *Climate Change 2021: The Physical Science Basis.*
591 Contribution of Working Group I to the Sixth Assessment Report of the Intergovernmental Panel on Climate Change.

592



593 Cambridge University Press, Cambridge, United Kingdom and New York, NY, USA, pp. 1211–1362.
594 <https://doi.org/10.1017/9781009157896.001>

595 Gallée, H., 1997. Air-sea interactions over Terra Nova Bay during winter: Simulation with a coupled atmosphere-polynya
596 model. *J. Geophys. Res. Atmospheres* 102, 13835–13849. <https://doi.org/10.1029/96JD03098>

597 Gallée, H., Schayes, G., 1994. Development of a Three-Dimensional Meso-γ Primitive Equation Model: Katabatic Winds
598 Simulation in the Area of Terra Nova Bay, Antarctica. *Mon. Weather Rev.* 122, 671–685. [https://doi.org/10.1175/1520-0493\(1994\)122<0671:DOATDM>2.0.CO;2](https://doi.org/10.1175/1520-0493(1994)122<0671:DOATDM>2.0.CO;2)

600 Ghafarian, F., Wieland, R., Lütschwager, D., Nendel, C., 2022. Application of extreme gradient boosting and Shapley
601 Additive explanations to predict temperature regimes inside forests from standard open-field meteorological data.
602 *Environ. Model. Softw.* 156, 105466. <https://doi.org/10.1016/j.envsoft.2022.105466>

603 Goelles, T., Bøggild, C.E., 2017. Albedo reduction of ice caused by dust and black carbon accumulation: a model applied to
604 the K-transect, West Greenland. *J. Glaciol.* 63, 1063–1076. <https://doi.org/10.1017/jog.2017.74>

605 Gorelick, N., Hancher, M., Dixon, M., Ilyushchenko, S., Thau, D., Moore, R., 2017. Google Earth Engine: Planetary-scale
606 geospatial analysis for everyone. *Remote Sens. Environ.* 202, 18–27. <https://doi.org/10.1016/j.rse.2017.06.031>

607 Hall, D. K., Salomonson, V. V., and Riggs, G. A.: MODIS/Terra Snow Cover Daily L3 Global 500m Grid. Version 6, Boulder,
608 Colorado, USA: NASA National Snow and Ice Data Center Distributed Active Archive Center [data set],
609 <https://doi.org/10.5067/MODIS/MOD10A1.006>, 2016.

610 Hersbach, H., Bell, B., Berrisford, P., Hirahara, S., Horányi, A., Muñoz-Sabater, J., Nicolas, J., Peubey, C., Radu, R.,
611 Schepers, D., Simmons, A., Soci, C., Abdalla, S., Abellán, X., Balsamo, G., Bechtold, P., Biavati, G., Bidlot, J.,
612 Bonavita, M., Chiara, G., Dahlgren, P., Dee, D., Diamantakis, M., Dragani, R., Flemming, J., Forbes, R., Fuentes, M.,
613 Geer, A., Haimberger, L., Healy, S., Hogan, R.J., Hólm, E., Janisková, M., Keeley, S., Laloyaux, P., Lopez, P., Lupu, C.,
614 Radnoti, G., Rosnay, P., Rozum, I., Vamborg, F., Villaume, S., Thépaut, J., 2020. The ERA5 global reanalysis. *Q. J. R. Meteorol. Soc.* 146, 1999–2049. <https://doi.org/10.1002/qj.3803>

615 Hofer, S., Tedstone, A.J., Fettweis, X., Bamber, J.L., 2017. Decreasing cloud cover drives the recent mass loss on the
616 Greenland Ice Sheet. *Sci. Adv.* 9.

617 Howat, I.M., Negrete, A., Smith, B.E., 2014. The Greenland Ice Mapping Project (GIMP) land classification and surface
618 elevation data sets. *The Cryosphere* 8, 1509–1518. <https://doi.org/10.5194/tc-8-1509-2014>

619 Huang, L., Kang, J., Wan, M., Fang, L., Zhang, C., Zeng, Z., 2021. Solar Radiation Prediction Using Different Machine
620 Learning Algorithms and Implications for Extreme Climate Events. *Front. Earth Sci.* 9.

621 Huber, P.J., 1964. Robust Estimation of a Location Parameter. *Ann. Math. Stat.* 35, 73–101.
622 <https://doi.org/10.1214/aoms/1177703732>

623 Ibrahem Ahmed Osman, A., Najah Ahmed, A., Chow, M.F., Feng Huang, Y., El-Shafie, A., 2021. Extreme gradient
624 boosting (Xgboost) model to predict the groundwater levels in Selangor Malaysia. *Ain Shams Eng. J.* 12, 1545–1556.
625 <https://doi.org/10.1016/j.asej.2020.11.011>

626 Ishfaque, M., Salman, S., Jadoon, K.Z., Danish, A.A.K., Bangash, K.U., Qianwei, D., 2022. Understanding the Effect of
627 Hydro-Climatological Parameters on Dam Seepage Using Shapley Additive Explanation (SHAP): A Case Study of
628 Earth-Fill Tarbela Dam, Pakistan. *Water* 14, 2598. <https://doi.org/10.3390/w14172598>

629 Jonsell, U., Hock, R., Holmgren, B., 2003. Spatial and temporal variations in albedo on Storglaciären, Sweden. *J. Glaciol.*
630 49, 59–68. <https://doi.org/10.3189/172756503781830980>

631 Keegan, K.M., Albert, M.R., McConnell, J.R., Baker, I., 2014. Climate change and forest fires synergistically drive
632 widespread melt events of the Greenland Ice Sheet. *Proc. Natl. Acad. Sci.* 111, 7964–7967.
633 <https://doi.org/10.1073/pnas.1405397111>

634 Khan, A.L., Xian, P., Schwarz, J.P., 2023. Black carbon concentrations and modeled smoke deposition fluxes to the bare-ice
635 dark zone of the Greenland Ice Sheet. *The Cryosphere* 17, 2909–2918. <https://doi.org/10.5194/tc-17-2909-2023>



637 Klein, A.G., Stroeve, J., 2002. Development and validation of a snow albedo algorithm for the MODIS instrument. *Ann.*
638 *Glaciol.* 34, 45–52. <https://doi.org/10.3189/172756402781817662>

639 Koo, Y., Xie, H., Kurtz, N.T., Ackley, S.F., Wang, W., 2023. Sea ice surface type classification of ICESat-2 ATL07 data by
640 using data-driven machine learning model: Ross Sea, Antarctic as an example. *Remote Sens. Environ.* 296, 113726.
641 <https://doi.org/10.1016/j.rse.2023.113726>

642 Lefebvre, F., Gallée, H., Ypersele, J.-P. van, Greuell, W., 2003. Modeling of snow and ice melt at ETH Camp (West
643 Greenland): A study of surface albedo. *J. Geophys. Res. Atmospheres* 108. <https://doi.org/10.1029/2001JD001160>

644 Li, J., Wu, C., Zhang, Y., Peñuelas, J., Liu, L., Ge, Q., 2024. Weakening warming on spring freeze–thaw cycle caused
645 greening Earth’s third pole. *Proc. Natl. Acad. Sci.* 121, e2319581121. <https://doi.org/10.1073/pnas.2319581121>

646 Liang, S., 2001. Narrowband to broadband conversions of land surface albedo I. *Remote Sens. Environ.* 76, 213–238.
647 [https://doi.org/10.1016/S0034-4257\(00\)00205-4](https://doi.org/10.1016/S0034-4257(00)00205-4)

648 Lundberg, S., Lee, S.-I., 2017. A Unified Approach to Interpreting Model Predictions.
649 <https://doi.org/10.48550/ARXIV.1705.07874>

650 Ma, M., Zhao, G., He, B., Li, Q., Dong, H., Wang, S., Wang, Z., 2021. XGBoost-based method for flash flood risk
651 assessment. *J. Hydrol.* 598, 126382. <https://doi.org/10.1016/j.jhydrol.2021.126382>

652 Ma, X., Fang, C., Ji, J., 2020. Prediction of outdoor air temperature and humidity using Xgboost. *IOP Conf. Ser. Earth
653 Environ. Sci.* 427, 012013. <https://doi.org/10.1088/1755-1315/427/1/012013>

654 MacGregor, J.A., Fahnestock, M.A., Colgan, W.T., Larsen, N.K., Kjeldsen, K.K., Welker, J.M., 2020. The age of surface-
655 exposed ice along the northern margin of the Greenland Ice Sheet. *J. Glaciol.* 66, 667–684.
656 <https://doi.org/10.1017/jog.2020.62>

657 McCutcheon, J., Lutz, S., Williamson, C., Cook, J.M., Tedstone, A.J., Vanderstraeten, A., Wilson, S.A., Stockdale, A.,
658 Bonneville, S., Anesio, A.M., Yallop, M.L., McQuaid, J.B., Tranter, M., Benning, L.G., 2021. Mineral phosphorus drives
659 glacier algal blooms on the Greenland Ice Sheet. *Nat. Commun.* 12, 570. <https://doi.org/10.1038/s41467-020-20627-w>

660 Meinander, O., Dagsson-Waldhauserová, P., Arnalds, O., 2016. Icelandic volcanic dust can have a significant influence on
661 the cryosphere in Greenland and elsewhere. *Polar Res.* <https://doi.org/10.3402/polar.v35.31313>

662 Moroni, B., Arnalds, O., Dagsson-Waldhauserová, P., Crochiani, S., Vivani, R., Cappelletti, D., 2018. Mineralogical and
663 Chemical Records of Icelandic Dust Sources Upon Ny-Ålesund (Svalbard Islands). *Front. Earth Sci.* 6, 415699.
664 <https://doi.org/10.3389/feart.2018.00187>

665 Moustafa, S.E., Rennermalm, A.K., Smith, L.C., Miller, M.A., Mioduszewski, J.R., Koenig, L.S., Hom, M.G., Shuman,
666 C.A., 2015. Multi-modal albedo distributions in the ablation area of the southwestern Greenland Ice Sheet. *The
667 Cryosphere* 9, 905–923. <https://doi.org/10.5194/tc-9-905-2015>

668 Munro, D.S., 1990. Comparison of Melt Energy Computations and Ablatometer Measurements on Melting Ice and Snow.
669 *Arct. Alp. Res.* 22, 153–162. <https://doi.org/10.2307/1551300>

670 Nagatsuka, N., Goto-Azuma, K., Tsushima, A., Fujita, K., Matoba, S., Onuma, Y., Dallmayr, R., Kadota, M., Hirabayashi,
671 M., Ogata, J., Ogawa-Tsukagawa, Y., Kitamura, K., Minowa, M., Komuro, Y., Motoyama, H., Aoki, T., 2021. Variations
672 in mineralogy of dust in an ice core obtained from northwestern Greenland over the past 100 years. *Clim. Past* 17, 1341–
673 1362. <https://doi.org/10.5194/cp-17-1341-2021>

674 Nkiruka, O., Prasad, R., Clement, O., 2021. Prediction of malaria incidence using climate variability and machine learning.
675 *Inform. Med. Unlocked* 22, 100508. <https://doi.org/10.1016/j.imu.2020.100508>

676 Noël, B., van de Berg, W.J., Lhermitte, S., van den Broeke, M.R., 2019. Rapid ablation zone expansion amplifies north
677 Greenland mass loss. *Sci. Adv.* 5, eaaw0123. <https://doi.org/10.1126/sciadv.aaw0123>

678 Riah, K., van Vuuren, D.P., Kriegler, E., Edmonds, J., O'Neill, B.C., Fujimori, S., Bauer, N., Calvin, K., Dellink, R.,
679 Fricko, O., Lutz, W., Popp, A., Cuaresma, J.C., Kc, S., Leimbach, M., Jiang, L., Kram, T., Rao, S., Emmerling, J., Ebi,
680 K., Hasegawa, T., Havlik, P., Humpenöder, F., Da Silva, L.A., Smith, S., Stehfest, E., Bosetti, V., Eom, J., Gernaat, D.,



681 Masui, T., Rogelj, J., Strefler, J., Drouet, L., Krey, V., Luderer, G., Harmsen, M., Takahashi, K., Baumstark, L.,
682 Doelman, J.C., Kainuma, M., Klimont, Z., Marangoni, G., Lotze-Campen, H., Obersteiner, M., Tabeau, A., Tavoni, M.,
683 2017. The Shared Socioeconomic Pathways and their energy, land use, and greenhouse gas emissions implications: An
684 overview. *Glob. Environ. Change* 42, 153–168. <https://doi.org/10.1016/j.gloenvcha.2016.05.009>

685 Ridder, K.D., Schayes, G., 1997. The IAGL Land Surface Model. *J. Appl. Meteorol. Climatol.* 36, 167–182.
686 [https://doi.org/10.1175/1520-0450\(1997\)036<0167:TILSM>2.0.CO;2](https://doi.org/10.1175/1520-0450(1997)036<0167:TILSM>2.0.CO;2)

687 Rohmer, J., Thieblemont, R., Le Cozannet, G., Goelzer, H., Durand, G., 2022. Improving interpretation of sea-level
688 projections through a machine-learning-based local explanation approach. *The Cryosphere* 16, 4637–4657.
689 <https://doi.org/10.5194/tc-16-4637-2022>

690 Ryan, J.C., Smith, L.C., van As, D., Cooley, S.W., Cooper, M.G., Pitcher, L.H., Hubbard, A., 2019. Greenland Ice Sheet
691 surface melt amplified by snowline migration and bare ice exposure. *Sci. Adv.* 5, eaav3738.
692 <https://doi.org/10.1126/sciadv.aav3738>

693 Shimada, R., Takeuchi, N., Aoki, T., 2016. Inter-Annual and Geographical Variations in the Extent of Bare Ice and Dark Ice
694 on the Greenland Ice Sheet Derived from MODIS Satellite Images. *Front. Earth Sci.* 4.
695 <https://doi.org/10.3389/feart.2016.00043>

696 Silva, S.J., Keller, C.A., Hardin, J., 2022. Using an Explainable Machine Learning Approach to Characterize Earth System
697 Model Errors: Application of SHAP Analysis to Modeling Lightning Flash Occurrence. *J. Adv. Model. Earth Syst.* 14,
698 e2021MS002881. <https://doi.org/10.1029/2021MS002881>

699 Stibal, M., Box, J.E., Cameron, K.A., Langen, P.L., Yallop, M.L., Mottram, R.H., Khan, A.L., Molotch, N.P., Chrimas,
700 N.A.M., Cali Quaglia, F., Remias, D., Smeets, C.J.P.P., Broeke, M.R., Ryan, J.C., Hubbard, A., Tranter, M., As, D.,
701 Ahlström, A.P., 2017. Algae Drive Enhanced Darkening of Bare Ice on the Greenland Ice Sheet. *Geophys. Res. Lett.* 44,
702 11,463–11,471. <https://doi.org/10.1002/2017GL075958>

703 Stroeve, J., 2001. Assessment of Greenland albedo variability from the advanced very high resolution radiometer Polar
704 Pathfinder data set. *J. Geophys. Res. Atmospheres* 106, 33989–34006. <https://doi.org/10.1029/2001JD900072>

705 Tan, W., Wei, C., Lu, Y., Xue, D., 2021. Reconstruction of All-Weather Daytime and Nighttime MODIS Aqua-Terra Land
706 Surface Temperature Products Using an XGBoost Approach. *Remote Sens.* 13, 4723. <https://doi.org/10.3390/rs13224723>

707 Tang, Y., Duan, A., Xiao, C., Xin, Y., 2022. The Prediction of the Tibetan Plateau Thermal Condition with Machine
708 Learning and Shapley Additive Explanation. *Remote Sens.* 14, 4169. <https://doi.org/10.3390/rs14174169>

709 Tedesco, M., Doherty, S., Fettweis, X., Alexander, P., Jeyaratnam, J., Stroeve, J., 2016. The darkening of the Greenland ice
710 sheet: trends, drivers, and projections (1981–2100). *The Cryosphere* 10, 477–496. <https://doi.org/10.5194/tc-10-477-2016>

711 Tedstone, A.J., Cook, J.M., Williamson, C.J., Hofer, S., McCutcheon, J., Irvine-Fynn, T., Gribbin, T., Tranter, M., 2020.
712 Algal growth and weathering crust state drive variability in western Greenland Ice Sheet ice albedo. *The Cryosphere* 14,
713 521–538. <https://doi.org/10.5194/tc-14-521-2020>

714 Temenos, A., Temenos, N., Kaselimi, M., Doulamis, A., Doulamis, N., 2023. Interpretable Deep Learning Framework for
715 Land Use and Land Cover Classification in Remote Sensing Using SHAP. *IEEE Geosci. Remote Sens. Lett.* 20, 1–5.
716 <https://doi.org/10.1109/LGRS.2023.3251652>

717 Thomas, J.L., Polashenski, C.M., Soja, A.J., Marelle, L., Casey, K.A., Choi, H.D., Raut, J.-C., Wiedinmyer, C., Emmons,
718 L.K., Fast, J.D., Pelon, J., Law, K.S., Flanner, M.G., Dibb, J.E., 2017. Quantifying black carbon deposition over the
719 Greenland ice sheet from forest fires in Canada. *Geophys. Res. Lett.* 44, 7965–7974.
720 <https://doi.org/10.1002/2017GL073701>

721 Uetake, J., Naganuma, T., Hebsgaard, M.B., Kanda, H., Kohshima, S., 2010. Communities of algae and cyanobacteria on
722 glaciers in west Greenland. *Polar Sci.* 4, 71–80. <https://doi.org/10.1016/j.polar.2010.03.002>

723 Újvári, G., Klötzli, U., Stevens, T., Svensson, A., Ludwig, P., Vennemann, T., Gier, S., Horschinegg, M., Palcsu, L.,
724 Hippler, D., Kovács, J., Biagio, C.D., Formenti, P., 2022. Greenland Ice Core Record of Last Glacial Dust Sources and



725 Atmospheric Circulation. *J. Geophys. Res. Atmospheres* 127, e2022JD036597. <https://doi.org/10.1029/2022JD036597>

726 van Dalum, C.T., van de Berg, W.J., Lhermitte, S., van den Broeke, M.R., 2020. Evaluation of a new snow albedo scheme
727 for the Greenland ice sheet in the regional climate model RACMO2. <https://doi.org/10.5194/tc-2020-118>

728 van den Broeke, M., Box, J., Fettweis, X., Hanna, E., Noël, B., Tedesco, M., van As, D., van de Berg, W.J., van
729 Kampenhout, L., 2017. Greenland Ice Sheet Surface Mass Loss: Recent Developments in Observation and Modeling.
730 *Curr. Clim. Change Rep.* 3, 345–356. <https://doi.org/10.1007/s40641-017-0084-8>

731 van Kampenhout, L., Lenaerts, J.T.M., Lipscomb, W.H., Lhermitte, S., Noël, B., Vizcaíno, M., Sacks, W.J., van den Broeke,
732 M.R., 2020. Present-Day Greenland Ice Sheet Climate and Surface Mass Balance in CESM2. *J. Geophys. Res. Earth
733 Surf.* 125, e2019JF005318. <https://doi.org/10.1029/2019JF005318>

734 Vermote, E.F., El Saleous, N.Z., Justice, C.O., 2002. Atmospheric correction of MODIS data in the visible to middle
735 infrared: first results. *Remote Sens. Environ.* 83, 97–111.

736 Vermote, E.F., Tanre, D., Deuze, J.L., Herman, M., Morcette, J.-J., 1997. Second Simulation of the Satellite Signal in the
737 Solar Spectrum, 6S: an overview. *IEEE Trans. Geosci. Remote Sens.* 35, 675–686. <https://doi.org/10.1109/36.581987>

738 Vermote, E., and Wolfe, R.: MOD09GA MODIS/Terra Surface Reflectance Daily L2G Global 1km and 500m SIN Grid V006,
739 NASA EOSDIS Land Processes DAAC [data set], <https://doi.org/10.5067/MODIS/MOD09GA.006>, 2015.

740 Wang, S., Tedesco, M., Alexander, P., Xu, M., Fettweis, X., 2020. Quantifying spatiotemporal variability of glacier algal
741 blooms and the impact on surface albedo in southwestern Greenland. *The Cryosphere* 14, 2687–2713.
742 <https://doi.org/10.5194/tc-14-2687-2020>

743 Wang, Z., Bovik, A.C., Sheikh, H.R., Simoncelli, E.P., 2004. Image quality assessment: from error visibility to structural
744 similarity. *IEEE Trans. Image Process.* 13, 600–612. <https://doi.org/10.1109/TIP.2003.819861>

745 Ward, J.L., Flanner, M.G., Bergin, M., Dibb, J.E., Polashenski, C.M., Soja, A.J., Thomas, J.L., 2018. Modeled Response of
746 Greenland Snowmelt to the Presence of Biomass Burning-Based Absorbing Aerosols in the Atmosphere and Snow. *J.
747 Geophys. Res. Atmospheres* 123, 6122–6141. <https://doi.org/10.1029/2017JD027878>

748 Warren, S.G., Brandt, R.E., Grenfell, T.C., 2006. Visible and near-ultraviolet absorption spectrum of ice from transmission
749 of solar radiation into snow. *Appl. Opt.* 45, 5320. <https://doi.org/10.1364/AO.45.005320>

750 Warren, S.G., Wiscombe, W.J., 1980. A model for the spectral albedo of snow. II: Snow containing atmospheric aerosols. *J.
751 Atmospheric Sci.* 37, 2734–2745.

752 Whicker, C.A., Flanner, M.G., Dang, C., Zender, C.S., Cook, J.M., Gardner, A.S., 2022. SNICAR-ADv4: a physically based
753 radiative transfer model to represent the spectral albedo of glacier ice. *The Cryosphere* 24.

754 Whicker-Clarke, C.A., Antwerpen, R., Flanner, M.G., Schneider, A., Tedesco, M., Zender, C.S., 2024. The Effect of
755 Physically Based Ice Radiative Processes on Greenland Ice Sheet Albedo and Surface Mass Balance in E3SM. *J.
756 Geophys. Res. Atmospheres* 129, e2023JD040241. <https://doi.org/10.1029/2023JD040241>

757 Wientjes, I.G.M., Oerlemans, J., 2010. An explanation for the dark region in the western melt zone of the Greenland ice
758 sheet. *The Cryosphere* 4, 261–268. <https://doi.org/10.5194/tc-4-261-2010>

759 Wientjes, I.G.M., Van De Wal, R.S.W., Schwikowski, M., Zapf, A., Fahrni, S., Wacker, L., 2012. Carbonaceous particles
760 reveal that Late Holocene dust causes the dark region in the western ablation zone of the Greenland ice sheet. *J. Glaciol.*
761 58, 787–794. <https://doi.org/10.3189/2012JoG11J165>

762 Williamson, C.J., Cook, J., Tedstone, A., Yallop, M., McCutcheon, J., Poniecka, E., Campbell, D., Irvine-Fynn, T.,
763 McQuaid, J., Tranter, M., Perkins, R., Anesio, A., 2020. Algal photophysiology drives darkening and melt of the
764 Greenland Ice Sheet. *Proc. Natl. Acad. Sci.* 117, 5694–5705. <https://doi.org/10.1073/pnas.1918412117>

765 Wiscombe, W.J., Warren, S.G., 1980. A model for the spectral albedo of snow. I: Pure Snow. *J. Atmospheric Sci.* 37, 2712–
766 2733.

767 Yue, C., Zhao, L., Wolovick, M., Moore, J.C., 2021. Greenland Ice Sheet Surface Runoff Projections to 2200 Using Degree-
768 Day Methods. *Atmosphere* 12, 1569. <https://doi.org/10.3390/atmos12121569>



769 Zuo, Z., Oerlemans, J., 1996. Modelling albedo and specific balance of the Greenland ice sheet: calculations for the Søndre
770 Strømfjord transect. *J. Glaciol.* 42, 305–317. <https://doi.org/10.3189/S0022143000004160>
771



772 **Appendix A**

773 **Model parameters for Random Forest**

774 We perform a hyper-parameter search and find the Random Forest configuration with the best performance using a mean
775 squared error loss function and bootstrap sampling. The configuration includes number of trees in the forest (75), minimum
776 number of samples needed to split a node (15), minimum number of samples needed at each leaf node (8), method to determine
777 the number of considered features for the best split (square root of number of features), maximum tree depth (25).
778

779 **Model parameters for PySR**

780 The PySR architecture uses a Random Forest model for feature selection to build the symbolic expression. We set the
781 maximum number of features to seven, which yields the following set: near-surface temperature, runoff, shortwave downward
782 radiation, meridional wind, surface height, surface slope, surface aspect. We choose a range of potential operators $O_n^{(x,y)}$ with
783 varying complexity n applied to $(x, y) \in \mathbb{R}^2$:

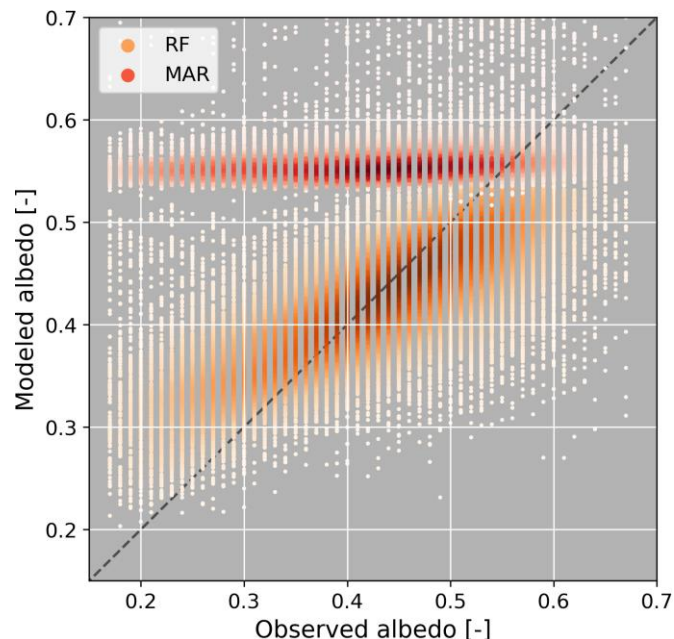
784 $O_3^{(x,y)} = [x + y, x - y, -x, x \cdot y, x^2]$

786 $O_6^{(x,y)} = [x/y, |x|, \sqrt{x}, x^3]$

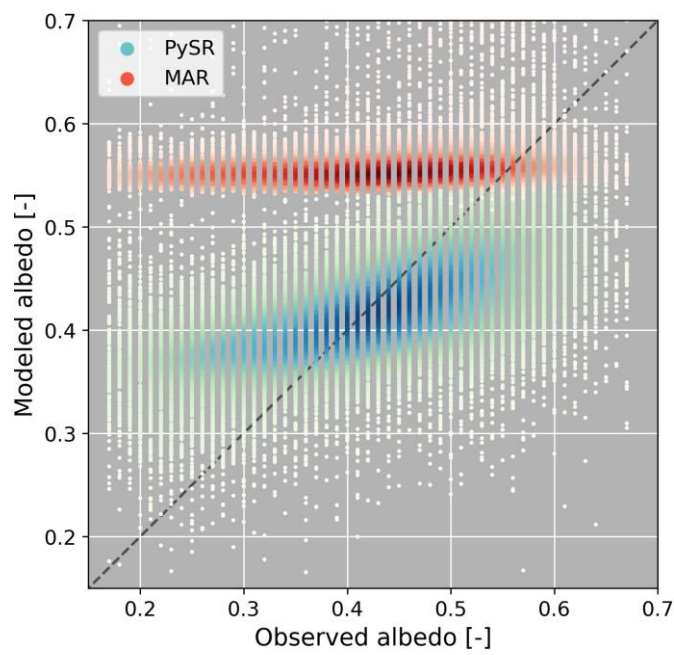
787 $O_9^{(x,y)} = [e^x, \ln(x), \log_2(x), \log_{10}(x), \sin(x), \cos(x), \tan(x), \sinh(x), \cosh(x), \tanh(x)]$

789 $O_{27}^{(x,y)} = [x^y, \tan(x), \operatorname{asinh}(x), \operatorname{acosh}(x), \operatorname{atanh}(x)]$

788
790 Operators with low complexity are preferred by the PySR algorithm in building the symbolic expression and we set the
791 maximum complexity to 70. The best results are obtained when we use 10,000 random samples from the training data set (JJA
792 in 2000-2019) and restrict the model to run for 400 iterations or 18 hours, whichever occurs first. Other parameters include a
793 population size of 400, each with 100 samples, and 400 mutations to run, per 10 samples, per iteration.



794
795 **Figure A1: Correlation between MODIS-derived ice albedo (x-axis) and ice albedo modeled with MAR (reds) and ice albedo modeled**
796 **with Random Forest (oranges). The dashed line represents the 1:1 line.**



798
799 **Figure A2: Correlation between MODIS-derived ice albedo (x-axis) and ice albedo modeled with MAR (reds) and ice albedo modeled**
800 **with PySR (green-blues). The dashed line represents the 1:1 line.**

801

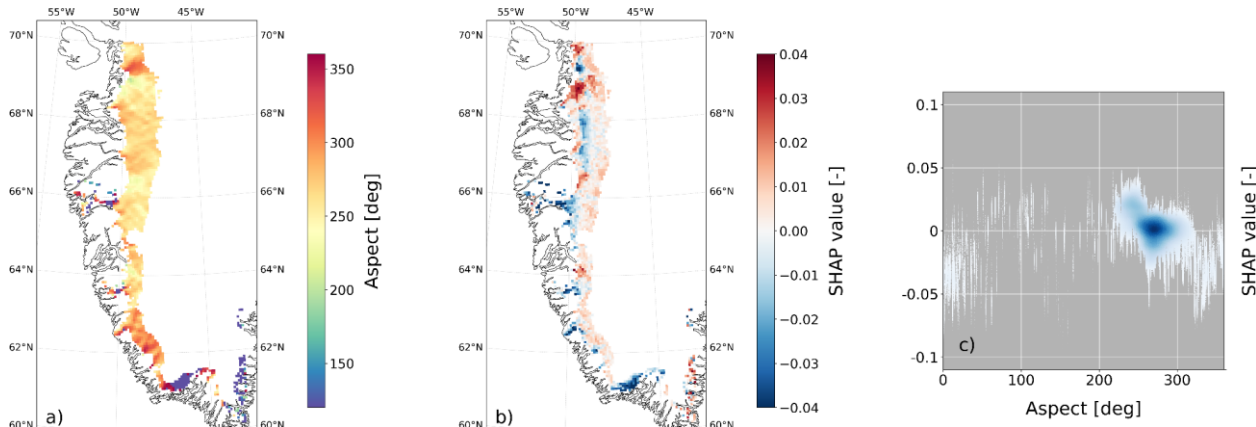


Figure A3: a) aspect, b) SHAP values for aspect, and c) their correlation. The maps show the average over JJA in 2020-2021.

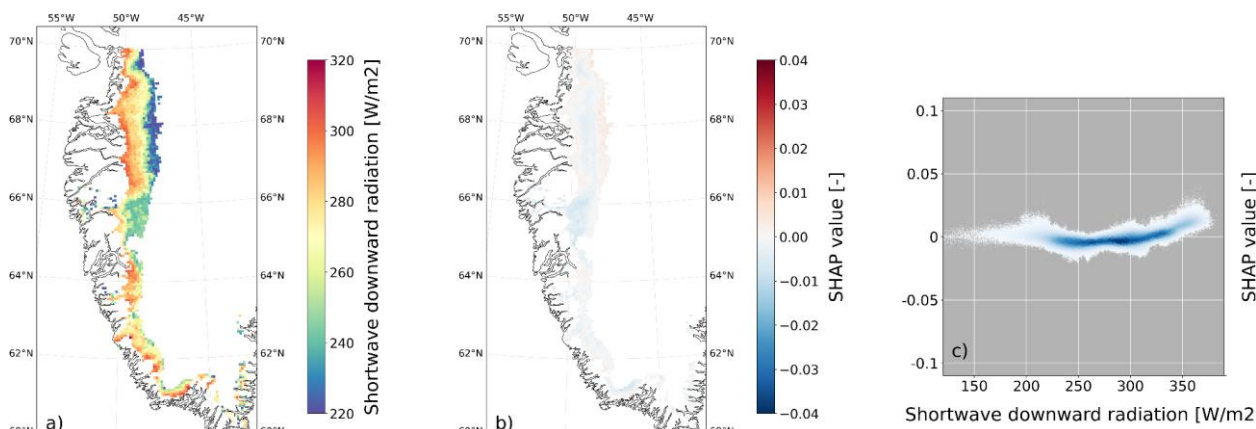


Figure A4: a) shortwave downward radiation, b) SHAP values for shortwave downward radiation, and c) their correlation. The maps show the average over JJA in 2020-2021.